Universidad Nacional Autónoma de México

Facultad de Ciencias

STUDY OF ACOUSTIC LEVITATION FORCES WITH OPTICAL LEVITATION

T E S I S

QUE PARA OBTENER EL TÍTULO DE:

Físico

P R E S E N T A :

Pablo Adrian Hernandez Munguia

TUTORES

Javier Tello Marmolejo
Alejandro Vásquez Arzola

Ciudad Universitaria, CDMX, 2023

1. Datos del alumno

   Hernandez
   Munguia
   Pablo Adrian
   +52 55 47659098
   Universidad Nacional Autóonoma de México
   Facultad de Ciencias
   Física
   415131832

2. Datos del tutor

   Dr.
   Alejandro
   Vásquez
   Arzola

3. Datos del sinodal 1

   Dra.
   Karen Patricia
   Volke
   Sepúlveda

4. Datos del sinodal 2

   Dr.
   Ricardo
   Méndez
   Fragoso

5. Datos del sinodal 3

   Dr.
   Pablo Luis
   Rendón
   Garrido

6. Datos del sinodal 4

   Dr.
   Victor Ulises Lev
   Contreras
   Loera

7. Datos del trabajo escrito

   Study of acoustic levitation forces with optical levitation
   46p
   2022

This work was performed under the supervision of Javier Tello Marmolejo and Dr. Dag Hanstorp at the University of Gothenburg, with the financial support of the Linnaeus-Palme Foundation.

A mis padres, que siempre han estado ahí para mí.

Resumen

Las técnicas de levitación acústica y óptica permiten mantener pequeñas partículas en el aire mediante el uso de ondas sonoras y luz láser, respectivamente. La levitación acústica puede producirse mediante un campo ultrasónico de ondas estacionarias, en el que partículas milimétricas quedan atrapadas dentro de los nodos de presión. La levitación óptica puede utilizarse como herramienta para medir fuerzas hasta escalas de femtonewtons, utilizando micropartículas levitadas como partículas prueba. Recientemente se han utilizado pinzas ópticas para medir campos acústicos y crear trampas combinadas *sono-ópticas* en medios microfluídicos. Sin embargo, aún no se ha explorado la levitación óptica como herramienta para medir campos de levitación acústica en aire. A diferencia de otros métodos para medir campos acústicos, el uso de levitación óptica permite medir fuerzas directamente sin perturbaciones mecánicas sobre el campo.

Esta tesis presenta un montaje experimental en el que se utilizan microesferas de sílice levitadas ópticamente como partículas prueba para medir el campo de fuerzas producido por un levitador acústico (AL, por sus siglas en inglés). El montaje permite el desplazamiento micrométrico del AL con respecto a la trampa óptica, de manera que la fuerza acústica puede medirse a lo largo de un volumen de unos pocos centímetros que contiene varios nodos de presión.

Un mapa de fuerzas de los nodos centrales del AL es obtenido mediante un barrido sobre un rango de posiciones sobre el eje de simetría del AL. Se mapean las componentes axial y radial, revelando las posiciones de los nodos y antinodos. También se muestra que la fuerza acústica aumenta cuadráticamente con la amplitud de la señal de entrada del AL, lo cual concuerda con literatura sono-óptica previa. Adicionalmente, se muestra que el campo del AL ejerce torcas sobre las microesferas. Estas torcas pueden controlarse modificando la amplitud del campo acústico y dependen de la ubicación de la partícula dentro del campo.

El uso de los conocimientos aquí adquiridos puede conducir a estudios más amplios y eficientes de campos de levitación acústica, dando lugar, por ejemplo, a mapas de fuerza de alta resolución en 2D y 3D.

La continuación de este trabajo podría conducir a potenciar características complementarias de las levitaciones óptica y acústica en un único sistema, ampliando su alcance en cuanto al tamaño de partícula. En pocas palabras, este trabajo podría servir como un peldaño en el camino hacia la sono-óptica en aire.

Abstract

Acoustic and optical levitation techniques allow holding small particles in midair by use of sound waves and laser light, respectively. Acoustic levitation can be produced through a standing-wave ultrasonic field, in which millimetric particles become trapped within the pressure nodes. Optical levitation can be used as a tool to measure forces down to the femtonewton scale by using levitated micro-particles as probes. Optical tweezers have been recently used to probe acoustic fields and create combined *sono-optical* traps in microfluidic environments. However, optical levitation as a tool to measure acoustic levitation fields in air has not been explored yet. Unlike other methods to measure acoustic fields, the use of optical levitation enables the direct measurement of forces without mechanically disturbing the field.

This thesis presents an experimental setup that uses optically levitated silica microspheres as probes for measuring the force field produced by an acoustic levitator (AL). The setup enables micrometric displacement of the AL with respect to the optical trap so that the acoustic force can be measured throughout a centimetre-scale volume containing several pressure nodes.

A force map of the AL central nodes is obtained by scanning along a range of positions at the symmetry axis of the AL. The axial and radial components are mapped, revealing the locations of the nodes and antinodes. It is also shown that the acoustic force increases quadratically with the amplitude of the AL input signal, which is in agreement with previous sono-optical literature. Additionally, it is shown that the AL field exerts torques on the microspheres. These torques can be controlled by modifying the amplitude of the acoustic field and are dependent on the particle's location within the field.

Using the knowledge acquired here can lead to broader and more efficient studies of acoustic levitation fields, resulting, for example, in 2D and 3D high-resolution force maps.

Continuation of this work could lead to exploiting complementary features of optical and acoustic levitation in a single system, expanding their trapping size-range. In short, this work could serve as a stepping stone toward sono-optics in air.

Acknowledgements

The journey to completing this thesis has been influenced by many individuals as well as some institutions. Here I will try to acknowledge the most critical ones since mentioning everyone would take too many pages.

First and foremost, my greatest gratitude to Javier Tello Marmolejo, who, in the first place, pushed me to go to Sweden and do my thesis project there. Thank you for guiding me and keeping an eye on my work in such an understanding and patient way. And most importantly, thank you for being a good friend. The past year was life-changing for me, and I owe it to you in many ways.

Thanks to Dag Hanstorp and Remigio Cabrera for their advice and for trusting me to be a part of the Linneaus-Palme program and have this invaluable experience at the University of Gothenburg. I also want to express my admiration to Dag for the fantastic work leading a research group with such a great atmosphere. I feel very fortunate to have been a part of it.

Thanks to Oscar and Janne for their advice and the good chats in the lab.

Special thanks to Mats, who spent many hours providing critical help to make the LabView program work properly.

Thanks to Andreas for all the help and advice with and around the acoustic levitators.

Thanks to Johann Jellstam, who manufactured the acoustic levitators I used and provided the design files.

Thanks to Rich, Sebastian, David and Chaytania for all the helpful advice and insights on my research.

Special thanks to Hinduja for her friendly support and collaboration in some of my experiments, as well as to Andrea for the hours we spent working alongside each other. I want to thank both of you for your friendship during my last months in Göteborg.

To Miranda, Ludi, Yogeshwar, Annie, Megha, Veena, Rachel, Keerthana, Meera, Jonas, Ademir, Victor and everyone mentioned above, thank you for the conversations and fun times during lunch breaks, fika sessions and other activities.

Thanks to Dani and Hirepan for being like a family to me throughout my stay in Sweden. I hold you in my heart. And, of course, to the extended family: Laura, Javi, Karen, Emiliano, Adri, Simon and Sean, thank you for welcoming us into the coolest Mexican family in Göteborg.

Alejandro Vásquez Arzola had the kindness of accepting to be my supervisor back at UNAM, and I want to express my gratitude for that. I appreciate all your feedback on my project and thesis, as well as your support with all the paperwork. I also want to thank my thesis jury members for the time and effort dedicated to reviewing my work and for their valuable comments. I am deeply grateful to have the opportunity of being evaluated by a group of experts who have truly inspired me in different ways on my journey through optics and acoustics.

I am also immensely grateful for the experiences and opportunities I have had as a student at UNAM. During this stage, I have had the privilege of learning from brilliant professors and have also been blessed with the company of many great classmates and friends. Although I wish I could express my gratitude to every single one, I will try to acknowledge some of my dearest ones with little hope of avoiding unfairness. To my dear friend Toño, who became a support that I never expected to get. You single-handedly opened many doors for me, and I can never thank you enough for that. To León, Anastassia and Roque, buddies of adventures and games. To José and Siddartha who pushed me to be a better version of myself. To Dunia, Karen, Bofo and Cass, that shared many great laughs with me. To Lucerro, I am glad that we keep checking up on each other after all these years. And to Ari, Cedric, Lechu, Williams, Kike, Abraham, Dianita, Ivette, Scarlett, Ivan, Ireri, Juanito, Cristy, Tania, los jóvenes David and Dardón, Raúl, Coria and Jenny. In addition, I want to recognize all the taxpayers in Mexico that allow many of us to have an exceptional education in this academic institution.

Finally, but no less warmly, I would like to thank all the rest of my friends and family who supported me in all kinds of situations. Most importantly, I could not have done any of this without all the unconditional love and support my parents have given me throughout my life.

Contents

1 Introduction

The problem of levitating matter has been approached and solved by physicists for about a century now [1, 2], but it is still a subject of research. The main challenge in levitation is not to find forces that act on matter in an invisible or contact-free way, since those are abundant and well known in physics, but to set such a force field in a way that it can stably counteract the weight of an object. Several levitation techniques exist today, including aerodynamic, acoustic, electric, magnetic, and1 optical levitation, along with numerous exciting research and applications, ranging from magnetic levitation trains to creating Star Wars-like volumetric displays [2–6].

The following work deals with measuring the forces present in acoustic levitation by using optical levitation as a measuring tool. Both of these levitation techniques are produced through the exertion of radiation pressure by a wave (a sound wave or a light wave, respectively) on a small particle. Optical and acoustic waves are able to produce not only levitation but also *trapping*, i.e. not only maintaining the particle in midair[1] but fixing it at some equilibrium position and restricting displacements in any direction. While optical levitation can be used to trap objects ranging from atoms up to micron-size particles in air or vacuum, acoustic levitation has a working scope from hundreds of micrometres to a few centimetres in size. Hereunder is a brief historical background of acoustic and optical levitation, along with some current outlooks relevant to this work.

1.1 Acoustic and optical levitation

The trapping capabilities of acoustic standing waves have been known since 1866 [7] and acoustic levitation was first reported in 1933 by Bucks and Müller [8]. They levitated alcohol droplets in a standing wave produced by an ultrasonic vibrating rod and a reflecting wall. In subsequent decades, acoustic levitation research was mostly focused on spatial applications like manipulating liquids in microgravity [9].

Unlike most levitation methods, acoustic levitation does not require materials with special properties and is non-intrusive. Solids, liquids, and even insects can be levitated acoustically. Despite this, acoustic levitation methods did not undergo wide adoption until recently, mainly because of the technical complications and cost of the devices needed [10].

[1] Trapping can also occur in liquid media and sometimes still be called levitation. Here the medium is always assumed to be air unless otherwise specified.

In the last decade, the emergence of multi-emitter acoustic levitators triggered a lot of new developments in the field, favouring a transition to using more affordable, lower-power transducers [11].

In 2017 Asier Marzo and collaborators introduced a multi-emitter acoustic levitator design called the *TinyLev*, with the goal of "democratizing" acoustic levitation [12]. This design uses two opposite arrays of ultrasonic transducers instead of an emitter-reflector pair to create a standing wave field. Moreover, the arrays are focused into the central axis to increase the trapping efficiency, producing a stronger field around the central nodes. This thesis might not have been possible without the development of the TinyLev, since the levitators I had available to produce an acoustic trapping field were all inspired by it.

Nowadays, trapping acoustic fields can also be produced without standing waves [13]. For example, vortex beams capable of levitating small particles can be produced by manipulating the individual phases of transducers in a single-sided array [14]. All the recent advancements have made it possible not only to trap particles in a fixed position but to manipulate them in several ways. Millimetric and sub-millimetric particles can be trapped, translated in 3D and rotated with acoustic levitation. The exertion of torques can be achieved by creating an acoustic vortex, among other methods. However, this is still an active research field.

Although several applications of acoustic levitation exist [4, 11, 15], they are still mostly limited to academic research. Some examples are: doing spectroscopy on levitated microalgae [16] or studying the atomization of levitated fuel droplets [17]. Multiple technical challenges are still to be overcome in order to achieve the full potential of acoustic levitation techniques [11]. For this, a deeper understanding of the dynamics of acoustic levitated particles is needed.

Optical levitation was pioneered in 1971 [18] by Arthur Ashkin and J. M. Dziedzic. At the time, the radiation pressure of light was a well-known phenomenon [19], but the advent of the laser in 1960 was a key factor that allowed its practical application. After some back-of-the-envelope calculations, Ashkin realized that the momentum exchange between light and matter could be observed by focusing a laser onto a micron-size particle [20]. He first demonstrated this with transparent latex particles immersed in water, discovering that not only does the laser propel the particle in the propagation direction, but it also pulls it towards the laser's axis [21]. This discovery allowed him to create the first *optical trap* (OT) using two opposing laser beams [21]. After that, he used a single vertical beam to levitate a particle in air, where gravity and the particle's inertia play a more prominent role [18]. The levitated particle remains trapped by the counteraction of gravity and the optical force.

Several years later, Ashkin et al. demonstrated that a strongly focused single beam could provide a very stable new kind of OT called the optical tweezer [22]. Optical tweezers can trap a considerable range of objects, most notably atoms and living bac-

teria, which led to the development of numerous applications, particularly in biology. Ashkin received a Nobel prize for his work on optical tweezers in 2018.

From the start, one of the main applications of optical levitation has been to measure external forces, like electric fields or drag forces, exerted on the trapped particles. Particles of size up to tens of microns can be optically levitated in air and vacuum. The smallness of these particles and the stiffness of the optical traps allow measuring forces with high accuracy down to the femtonewton scale. Other applications include using a levitated particle as a light point source to visualize the aberrations of a lens [23] or performing chemical analyses of the collision of two levitated droplets [24].

The aim of this thesis is to use optical levitation as a contactless measuring tool to study the forces of a standing-wave acoustic levitator (AL). The method involves setting up an OT for micro-particles inside a TinyLev-like AL.

Different experimental methods have been reported to study the fields produced by an AL. Visualization methods are common to make qualitative comparisons with field simulations. The simplest way to visualize the field is by trapping objects to see where the nodes are [25]. A more enlightening method is to use Schlieren optics, which enables one to visualize small changes in the density or the pressure of the medium as gradients in intensity or colour [26, 27]. Another option is placing a liquid surface along the AL axis, allowing one to visualize the nodes and antinodes as dips and bumps on the surface [28].

For more quantitative studies of an AL field, the acoustic pressure level can be directly measured in a fixed position using a microphone [29–33]. A scanning in position with the microphone produces 2D or 3D mappings of the acoustic pressure field. In some cases, the force exerted by the AL field has been measured directly by introducing a millimetric probe particle attached to some sensitive weighing balance and scanning through the field with it [34, 35].

The methods mentioned in the last paragraph suffer from some disadvantages. First, calculating forces from pressure values may not be a simple task since the theoretical study of acoustic radiation pressure can be very complex. The most common approach (using Gor'kov's potential) is only valid for particles much smaller than the acoustic wavelength [11], which is usually not the case. Second, introducing an object into the field, e.g. a probe, a microphone or a wire to attach the probe to a balance, originates absorption and reflections that deform the field locally, and the size of these "deforming" objects is usually comparable with the wavelength of the AL.

The approach presented here utilizes optical levitation to tackle these issues. The optically levitated particles used as probes to measure the acoustic field are small enough to be consistent with Gor'kov's theory and do not significantly distort the field.

1.2 Sono-optics

Optical trapping has been used previously, in a way similar to the intended here, to measure acoustic trapping fields that propagate in microfluidic environments [36–39]. Ritsch-Marte et al. recently adopted the term *sono-optical* for a device that combines optical and acoustic trapping to avoid confusion with acousto-optics or photoacoustics [40]. Furthermore, the combined effect of both fields has been exploited to create sono-optical traps in microfluidics.

By combining these two levitation techniques, it is possible to use complementary features of each in a single trap, thereby allowing for the manipulation of objects over a broader range of sizes. For example, one can use the acoustic field to trap an ensemble of particles and the optical trap to manipulate a single one of them with more precision.

To my best knowledge, the simultaneous use of acoustic and optical levitation has not been explored in a gaseous environment prior to this work. Further exploration of this topic has the potential to close the gap between acoustic and optical levitation and ultimately result in the development of the first sono-optical levitation trap.

2 Theoretical background

Optical and acoustic levitation result from the application of *radiation pressure* forces exerted by a wave on a small particle. Radiation pressure can be interpreted as the exchange of linear momentum between a wave and a particle, and it is regarded as a second-order phenomenon of both optical and acoustic waves [41].

On the optics side, a complete study of the interaction between an arbitrary light beam and a sufficiently symmetric particle is provided by the Generalized Lorenz-Mie Theory (GLMT) [42]. An acoustic counterpart for GLMT has also been developed [43]. However, simpler approximations are commonly used for certain regimes and specific conditions, which help gain physical insight and describe the forces involved with certain accuracy. This chapter includes a brief look at theoretical approaches that describe the forces generated by radiation pressure in the cases relevant to the present work, both in the optical and acoustic cases.

2.1 Optical trapping

Consider a light beam being scattered by a particle. When the wavelength λ of the trapping light beam is much larger than the diameter d of the particle ($\lambda \gg d$), the *Rayleigh regime* is satisfied. Under this regime, the particle can be treated as a point dipole under the effects of an electromagnetic-wave field. Examples in the Rayleigh regime include the trapping of atoms or viruses with visible light. On the other hand, if $\lambda \ll d$, the *geometrical optics* regime is valid. Geometrical optics are used for example, when trapping eukaryotic cells with near-infrared light. Within both approaches, the resultant radiation force can be divided into two main components called the scattering force, which typically points in the direction of propagation of the laser, and the gradient force pointing towards the highest intensity point of the beam.

Here we are interested in levitating solid transparent spheres of diameter $d = 24\,\mu$m with a Gaussian laser beam of wavelength $\lambda = 532\,$nm. Hence, only the geometrical optics approach is considered.

2.1.1 Geometrical Optics

Although light is classically known to be an electromagnetic wave, the minuteness of its wavelength allows neglecting its wave nature in many situations, giving rise to the abstraction of rays. *Geometrical light rays* can be defined as the orthogonal trajectories to the geometrical wave-fronts of an optical field [44]. A ray propagates in the direction of the Poynting vector.

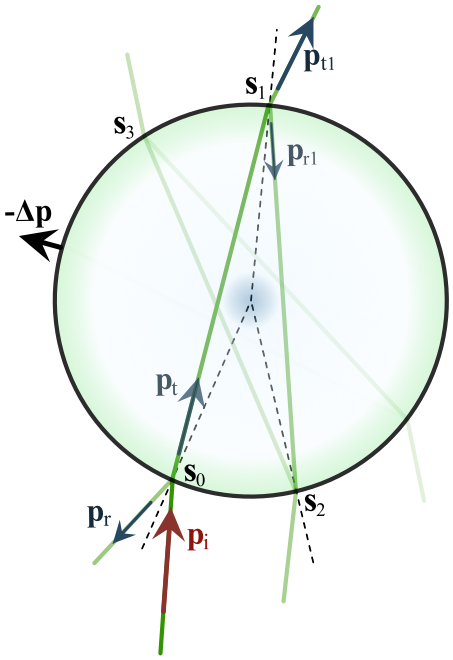

Figure 2.1: Momentum exchange of a single light ray with a spherical transparent particle. A light ray with momentum $\mathbf{p_i}$ (red vector) impinges on a sphere, and every time it reaches the sphere's surface, a scattering event ($\mathbf{s_j}$) occurs, producing new reflected and transmitted rays. All these rays account for a net change in linear momentum that the particle must counteract. It is assumed that the sphere has a higher refractive index than the medium.

Consider a single monochromatic light ray with linear momentum $\mathbf{p_i}$ impinging on a transparent spherical particle with negligible absorption. On the particle's interface, the ray gets split into a reflected and a transmitted ray, with momenta $\mathbf{p_r}$ and $\mathbf{p_t}$, respectively. When the transmitted ray reaches the surface of the sphere again, a second scattering event occurs, resulting in rays with momenta $\mathbf{p_{t1}}$ and $\mathbf{p_{r1}}$ (see Fig. 2.1). From then on, every reflected ray produces a new pair of internally reflected and transmitted rays. Overall, a net change in the linear momentum of the light ray can be obtained by considering all the resulting rays:

$$\Delta\mathbf{p} = -\mathbf{p_i} + \mathbf{p_r} + \sum_{j=1}^{\infty} \mathbf{p_{t}}_j \,. \tag{2.1}$$

By conservation of momentum, the particle experiences a change in momentum of $-\Delta\mathbf{p}$ due to the incident ray. In other terms, the force exerted by the ray on the particle is given by [45]

$$\mathbf{F}_{ray} = \frac{n_m}{c}\left(P_\mathbf{i}\hat{\mathbf{u}}_\mathbf{i} - P_\mathbf{r}\hat{\mathbf{u}}_\mathbf{r} - \sum_{j=1}^{\infty} P_{\mathbf{t}j}\hat{\mathbf{u}}_{\mathbf{t}j}\right) , \tag{2.2}$$

where n_m is the refractive index of the medium, c is the speed of light in vacuum, and every term inside the parenthesis is the product of a unitary vector and the power (P) carried by each corresponding ray in Eq. (2.1).

Notice that, because of the spherical symmetry, all the rays in Fig. 2.1 are in the same plane (the incidence plane of $\mathbf{p_i}$). Therefore it is customary to decompose $\mathbf{F}_{ray}$ into two components: the *scattering force* $\mathbf{F}_{s,ray}$ parallel to $\mathbf{p_i}$ and the *gradient force* $\mathbf{F}_{g,ray}$ perpendicular to $\mathbf{p_i}$ [45]. In order to obtain the total force from a full light beam, the contributions from each constituent ray must be summed:

$$\mathbf{F}_{opt} = \mathbf{F}_{scatt} + \mathbf{F}_{grad} = \sum_{rays} (\mathbf{F}_{s,ray} + \mathbf{F}_{g,ray}) \,,$$

where $\mathbf{F}_{scatt}$ and $\mathbf{F}_{grad}$ are the total scattering and gradient forces of the beam.

Most of the contributions to the optical forces are due to the first two scattering events since the reflection coefficient is usually very low. Furthermore, a ray's contribution is more significant at larger incident angles (except at angles very close to 90°) [46]. Therefore, when accounting for a full light beam, an analysis considering only a couple of rays, as in Fig. 2.2, can provide a good insight into the entire beam's effect.

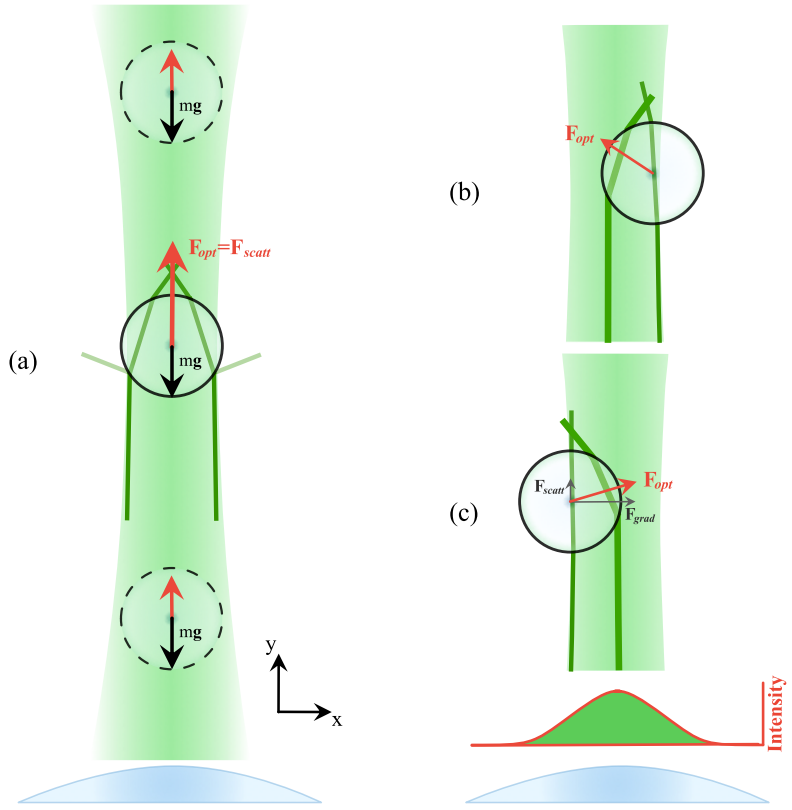

Figure 2.2: Forces in single-beam optical levitation trap. A Gaussian laser beam is focused with a lens, and a particle with a refractive index higher than the medium levitates near the beam waist. (a) If the particle is centred within the beam, the light gains momentum in the negative y-direction; hence the particle feels a force pushing it upwards. This optical force is stronger at the beam waist. (b)-(c) If the particle moves horizontally out of the axis of the beam, gradient forces become more significant and pull it back to the centre.

No matter how the particle scatters the light, conservation of momentum indicates that an upward scattering force will be produced. In a single-beam optical levitation setup, the power concentrated at the beam waist must produce a scattering force stronger than the particle weight. This force decreases gradually if the particle shifts away from the beam waist because fewer rays will pass through it. Hence an equilibrium position exists slightly above the focal point, where $\mathbf{F}_{scatt} = m\mathbf{g}$. In the horizontal direction, the gradient forces are responsible for keeping the particle in the light beam, as shown in Fig. 2.2(b) and (c).

Overall, gravity and the total scattering and gradient forces act in tandem to keep the particle trapped around the equilibrium position. The restoring nature of the net force allows modelling the optical levitation trap as a harmonic oscillator for small displacements in each dimension, namely

$$\mathbf{F}_{OT} = \mathbf{F}_{opt} + m\mathbf{g} \approx -(\kappa_x x, \kappa_y y, \kappa_z z)\,, \tag{2.3}$$

where (x, y, z) is the displacement vector of the particle and the origin of coordinates is taken at the equilibrium position of the trap. κ_x, κ_y and κ_z are the *trap stiffnesses* in the x-, y- and z-directions, i.e. the force per unit distance that the trap provides when the particle moves in the respective direction. Knowledge of the stiffness makes optical trapping a suitable tool for measuring external forces.

In the same sense, a harmonic potential can be approximated to describe the trapping potential in each direction, as

$$U_{x_i} = \frac{1}{2}\kappa_{x_i} x_i^2 + U_{0i}\,, \tag{2.4}$$

where $x_i = x, y, z$. Thus, a larger κ_{x_i} means a more "closed" parabola or a stiffer trap in x_i. The energy offset U_{0i} will be neglected when deriving to obtain the force.

In general, in a single-beam optical trap, the stiffness along the direction of propagation (κ_y) is smaller than the other two because of the restoring nature of the gradient forces, as opposed to the scattering force. If a highly-focused beam were used, e.g. by using a microscope objective, the gradient forces can become so significant in all directions even to counteract the scattering force. This principle is used to create an all-optical trap called the optical tweezers, in which gravity no longer plays a substantial role. However, even in optical tweezers, it typically holds that $\kappa_y < \kappa_x, \kappa_z$ [46].

2.1.2 Diffraction patterns

Optically levitated spherical particles scatter the beam's light in all directions. However, the scattering occurs mainly on the top and bottom poles along the propagation direction of the beam [47]. Levitated particles are often sufficiently small so that the light coming from these two scattering spots interferes, generating far-field diffraction patterns similar to those of a double slit. Hence, horizontal bright and dark fringes are seen in the transversal direction, as schematized in Fig. 2.3. The approximation of a double slit pattern can be employed to measure the size of the particle [47, 48]. On the other hand, along the path of the laser beam, the particle acts as a spherical obstacle creating diffraction rings above it [49].

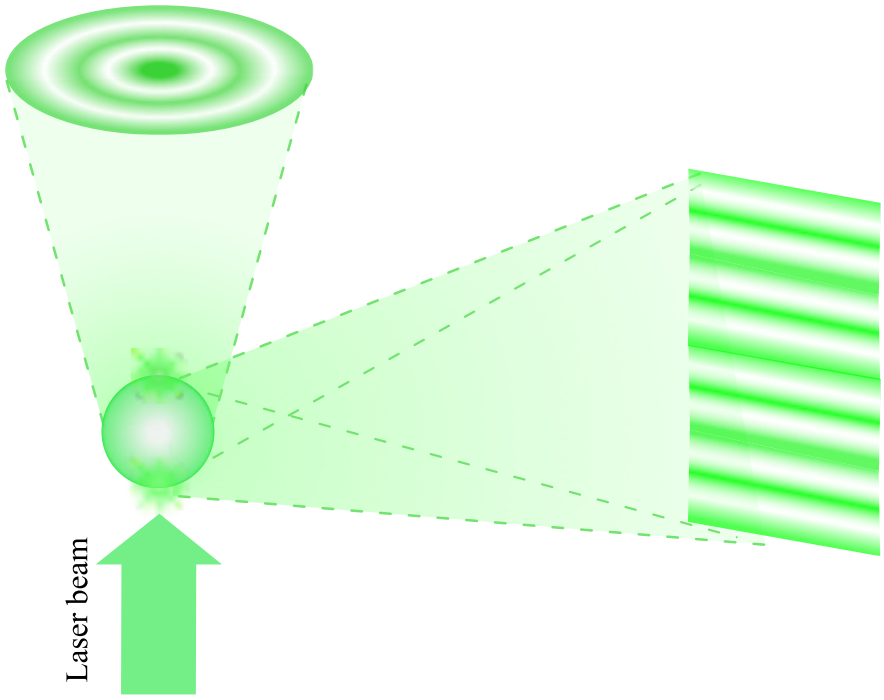

Figure 2.3: Far-field diffraction patterns generated by an optically levitated particle.

2.2 Acoustics and acoustic levitation

Acoustics studies the propagation of mechanical disturbances through a material medium (most typically a fluid). It is well known that the theoretical treatment of fluid dynamics can become highly complex. However, assuming that the acoustic waves under study have small amplitudes is a good enough approximation in numerous cases [50]. This *small-signal* approximation allows maintaining a certain theoretical simplicity.

Consider that the fluid medium, in the absence of a wave, has a constant density ρ_0 and pressure p_0 and that it is at rest ($\mathbf{v} = \mathbf{0}$), where $\mathbf{v}$ is the fluid velocity vector. When an acoustic wave is present, the total pressure, density and fluid velocity fields are slightly perturbed. We express this with respective first order perturbation fields, as follows:

$$\begin{aligned} p &= p_0 + p_1 \,, \\ \mathbf{v} &= \mathbf{v}_0 + \mathbf{v}_1 = \mathbf{v}_1 \,, \\ \rho &= \rho_0 + \rho_1 \,, \end{aligned}$$

with $|p_1| \ll p_0$, $|\rho_1| \ll \rho_0$ and $|\mathbf{v}| \ll c_0$, where c_0 is the speed of sound in the fluid [50]. Adding the assumptions of an inviscid and thermally nonconducting medium allows reducing the fundamental fluid equations to [13]:

a linearized continuity equation

$$\frac{\partial \rho_1}{\partial t} + \nabla \cdot (\rho_0 \mathbf{v}_1) = 0 \,, \tag{2.5}$$

a linearized momentum equation

$$\rho_0 \frac{\partial \mathbf{v}_1}{\partial t} = -\nabla p_1 \,, \tag{2.6}$$

and a linearized, isentropic equation of state

$$p_1 = c_0^2 \rho_1 \ . \tag{2.7}$$

Equations (2.5) to (2.7) provide a basis to derive the well-known linear wave equation:

$$\nabla^2 p_1 = \frac{1}{c_0^2} \frac{\partial^2 p_1}{\partial t^2} \ ,$$

which can be solved to obtain the *acoustic pressure* p_1 as a function of space and time for a given problem. Despite the broad scope of linear acoustics, which includes describing the general behaviour of standing waves (see the following section), it is not enough to describe the phenomenon of acoustic radiation pressure, which is the foundation for acoustic levitation.

2.2.1 Standing waves

Since the wave equation is a linear differential equation, the sum of two given solutions is also a solution. This property gives rise to the existence of *standing wave* solutions. A standing wave typically results from the superposition of two counterpropagating waves with the same frequency.

Consider the following counterpropagating harmonic plane waves emitted from sources located a distance $2d$ from each other:

$$p_+(x,t) = A\cos(k(x+d) - \omega t)\,,$$
$$p_-(x,t) = A\cos(k(x-d) + \omega t)\,,$$

where both waves have an amplitude A, angular frequency ω and a wave number $k = 2\pi/\lambda$, where λ is the wavelenght. Notice that the origin is located at the midpoint between the sources. When p_+ and p_- interfere, the resulting wave is

$$p_+ + p_- = 2A\cos(kx)\cos(\omega t - kd)\,. \tag{2.8}$$

This is a standing wave of double the amplitude of the constituent waves. Observe that the spatial phase, $\cos(kx)$, does not change with time, thus the *standing* nature of the wave. Moreover, the acoustic pressure in the points at which $\cos kx = 0$ remains null in time. These points are called the *nodes* of the standing wave. The points at which $\cos kx = 1$ are called the *antinodes* and are the points of maximum amplitude of the standing wave. The nodes (and antinodes) are separated by $\lambda/2$ (see Fig. 2.4).

2.2.2 Acoustic radiation pressure

Just as light, acoustic waves carry linear momentum that can be transferred to particles through the so-called *acoustic radiation force*. This nonlinear acoustic phenomenon can be described by incorporating second-order approximations into our analysis. Consider now the inclusion of the second-order perturbation (p_2) to the acoustic field:

$$p = p_0 + p_1 + p_2\,.$$

It turns out that the time-averaged *acoustic radiation pressure* can be obtained from first-order terms as [51]:

$$\langle p_2 \rangle = \frac{1}{2\rho_0 c_0^2}\langle p_1^2 \rangle - \frac{\rho_0}{2}\langle |\mathbf{v}_1|^2 \rangle\,. \tag{2.9}$$

Equation (2.9) gives the time-averaged acoustic radiation pressure for the case of high-frequency and time-harmonic fields, which is accurate in many applications of acoustic radiation pressure.

Finally, the *acoustic radiation force* exerted by an acoustic field on an object is calculated by the following surface integral:

$$\mathbf{F_{rad}} = -\int_S \langle p_2 \rangle d\mathbf{a}\,.$$

where S is the surface of the object.

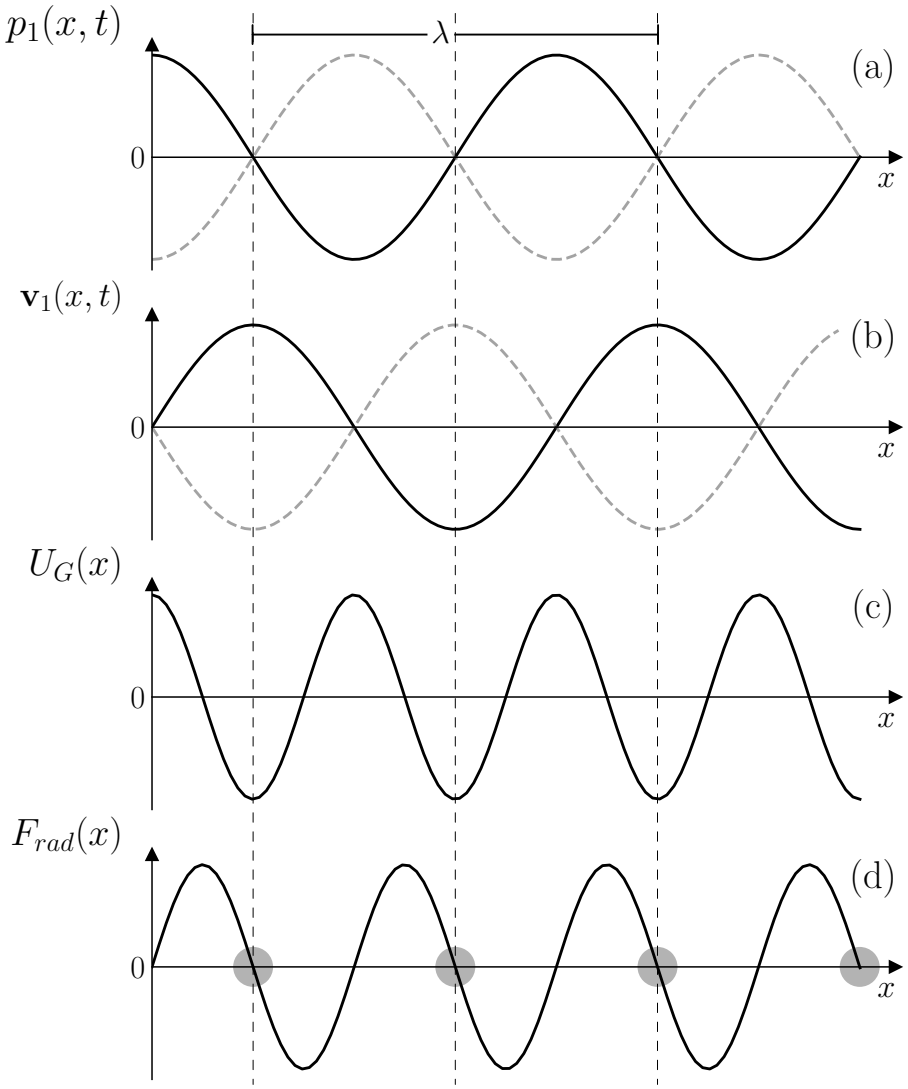

Figure 2.4: Acoustic radiation pressure due to a standing wave. The dashed vertical lines mark the position of the acoustic pressure nodes (a), which correspond to antinodes in the fluid velocity (b). These nodes correspond to minima in the Gor'kov potential (c), and to points where the radiation force cancels with negative slope (d).

2.2.3 Acoustic radiation of a standing wave on a small sphere

Acoustic levitation exists in the Rayleigh ($\lambda \gg d$) and Mie ($\lambda \approx d$) regimes [11]. Even ray approaches exist for cases where $\lambda \ll d$ [52]. The case of interest here is that of a spherical particle in the Rayleigh regime, for which there is an elegant and widely used solution proposed by L. P. Gor'kov [53]. He managed to express the radiation force in an ideal fluid as the gradient of the following potential:

$$U_G = 2\pi R^3 \left[\frac{f_1}{3\rho_0 c_0^2} \langle p_1^2 \rangle - \frac{f_2 \rho_0}{2} \langle |\mathbf{v}_1|^2 \rangle \right] , \tag{2.10}$$

where R is the particle radius and the factors f_1 and f_2 are dependent on the material properties of the particle and the medium. However, for solid particles levitated in air is safe to assume that $f_1 = f_2 = 1$.

Consider the acoustic standing wave given by[1]

$$p_1 = A \cos(kx) \cos(\omega t) .$$

Using Eq. (2.6) to obtain $\mathbf{v}_1$ and the relation $c_0 = \omega/k$ on Eq. (2.10) yields the potential

$$U_G = \frac{A^2 \pi R^3}{\rho_0 c_0^2} \left[\frac{\cos^2(kx)}{3} - \frac{\sin^2(kx)}{2} \right] . \tag{2.11}$$

Hence the radiation force exerted by p_1 on the particle is given by

$$\mathbf{F_{rad}} = -\nabla U_G = \frac{5\pi R^3 k A^2}{6\rho_0 c_0^2} \sin(2kx) \hat{\mathbf{x}} . \tag{2.12}$$

Figure 2.4 shows the plots of the results above, revealing that particles will get trapped in the pressure nodes of the acoustic wave. The pressure nodes correspond to the minima of the potential U_G, which is where the force graph crosses the axis with a negative slope. Notice that while Fig. 2.4(a) and Fig. 2.4(b) show the standing wave profile for a given time (e.g. $t = 0$), the expressions on Eqs. (2.11) and (2.12) are not time-dependent.

[1] Notice here that A corresponds to the peak-to-peak amplitude of the constituent travelling waves, in contrast to Eq. (2.8)

3 Methods

This chapter presents the experimental setup and methods used to study an optically levitated particle under the influence of an acoustic levitation field. Section 3.1 describes the optical levitation setup built and gives details of the acoustic levitator (AL) used. The position of the particles levitated with the optical trap (OT) is recorded using a position-sensitive detector (PSD). The functioning of the PSD and the consequent measurements conducted are explained in detail in section 3.2.

3.1 Experimental setup

Figure 3.1 shows the central part of the setup, where an optically levitated particle is seen as a bright green dot via the scattering of the intense laser light. While in the OT, the particle also interacts with the acoustic field produced by the red AL.

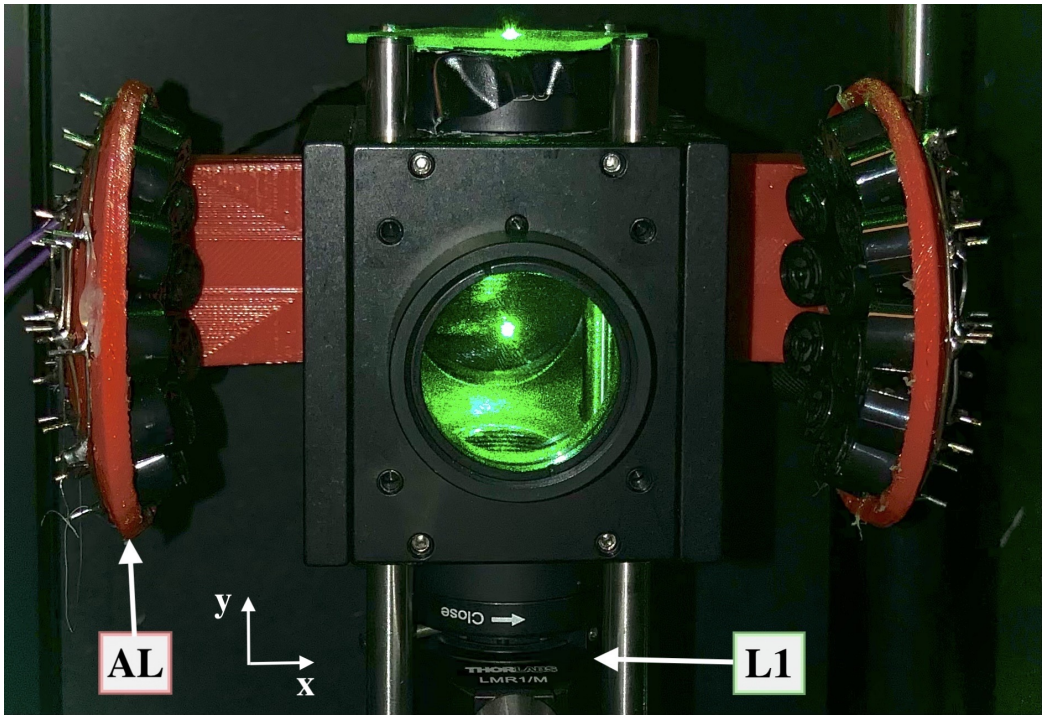

Figure 3.1: An optically levitated silica microsphere (bright spot in the centre) interacts with an acoustic potential. The optical trap (OT) consists of a vertical laser beam inciding from the bottom and focused with a lens (L1) into an optical cage. The two lateral windows of the cage remain open so that the acoustic levitator (AL) around the cage can produce a horizontal trapping acoustic field inside the cage. The AL is mounted on translation stages to be moved independently of the OT.

3.1.1 Optical trap (OT)

A 532 nm CW linearly polarized laser (Laser Quantum gem532) is directed upwards with a mirror and focused by a planoconvex lens (L1) of focal length $f = 40$ mm into a cubic optical cage with 5.10 cm sides, as shown in Fig. 3.2(a). Between 600-1000 mW of power from this vertically aligned laser beam are used to levitate silica microspheres. The focal point is set to be near the centre of the cage, ensuring enough free space for the acoustic fields to propagate around the stability position of trapped particles.

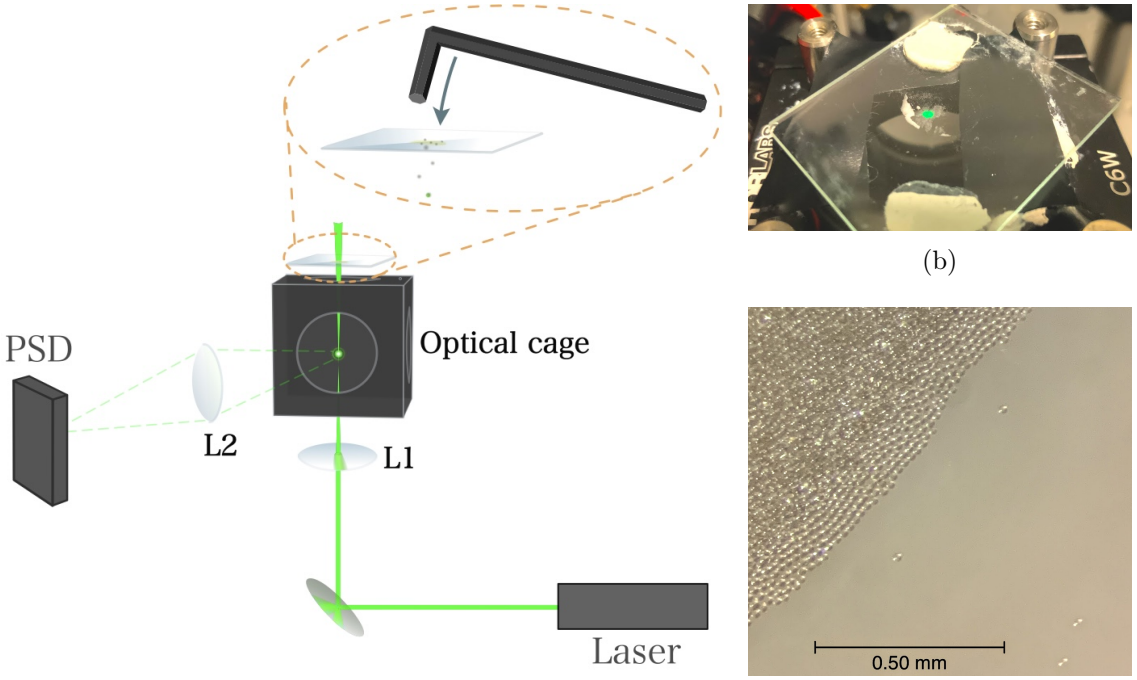

(a) (b) (c)

Figure 3.2: Optically trapping silica microspheres. (a) Diagram of the optical system. The 532 nm laser beam is focused with lens L1 to trap a particle inside an optical cage, and the light scattered by the particle is focused with lens L2 onto a position-sensitive detector (PSD). The top window of the cage is used to dispense the particles by tapping the glass plate with a hex key. (b) Picture of the glass plate set on top of the OT. In the centre some of the particles (SiO_2 microspheres) are lighted with the laser. (c) Particles stuck to the glass plate, observed under the microscope.

The optical cage can be isolated from air currents by installing transparent windows on each side. However, the two lateral windows must remain open for the AL waves to propagate inside[1]. The rest of the cage is maintained closed. Some cardboard walls are placed around the setup to improve the isolation as well.

[1]It was observed that having the AL turned off around the cage improves the ability to trap optically, as opposed to having completely unblocked windows.

Dispensing particles

Figure 3.2(c) exhibits a microscope view of the particles used: silica (SiO_2) microspheres of $24.28 \pm 1.06\,\mu m$ diameter and $1.85\,g/cm^3$ density (MicroParticles GmbH SiO_2-R-SC157). A small droplet of the particles' aqueous suspension is deposited on a thick glass slide, then left to dry or heated with a heat gun to accelerate the evaporation. This process results in a thin coating of particles stuck to the glass. The slide is then placed on top of the optical cage with the bulk of particles centred and facing down so that the laser beam hits some of them directly. With the OT turned on and the AL off, the glass slide is lightly tapped from above with a hex key, making some particles detach from the bulk and fall down, as highlighted in Fig. 3.2(a). Most falling particles do not align with the laser beam and land on the bottom window of the cage. However, from time to time, one falls right into the laser beam waist to get decelerated and trapped by the OT.[2]

At times, the particles overly stick to the glass plate. To help them unstick and drop as intended in such cases, it is convenient to softly scratch or directly tap the bulk of particles before dispensing. Additionally, the glass slide is attached to the cage with some sticky paste (see Fig. 3.2(b)) to avoid ricochets when tapping and to keep the upper window adequately closed.

3.1.2 Acoustic levitator (AL)

The AL used for this work was constructed by J. Jellstam [28] and is shown in Fig. 3.3. The design is an adaptation of the TinyLev [12] that locates both arrays of transducers on the inner surface of a single sphere (see Fig. 3.3(a)), in this case, with a diameter D = 117 mm. Each array consists of 18 transducers arranged into two concentric circles of radii 28.375 mm and 58.5 mm. The component transducers are manufactured to have a centre frequency of 40 ± 1 kHz.

The AL is oriented to have its axis aligned with the x-direction (perpendicular to the OT laser beam, see Figs. 3.1 and 3.4) and is mounted on translation stages so that it can be displaced in 3D with micrometric precision. Motorized translators (Thorlabs MTS50/M-Z8) are used for the x- and z-directions, and a manual translation stage for the y-direction (parallel to the OT laser beam).

Input signal

The acoustic field produced by the transducers in an acoustic levitator is controlled through electric AC signals. These signals must be amplified in order to provide enough power for levitation. TinyLev-type levitators need above 10 V peak-to-peak

[2] More than one particle can get trapped at a time. This can be recognized as a change in stability position (since the mass is larger) or empirically by looking at the far-field diffraction patterns, as shown in [54].

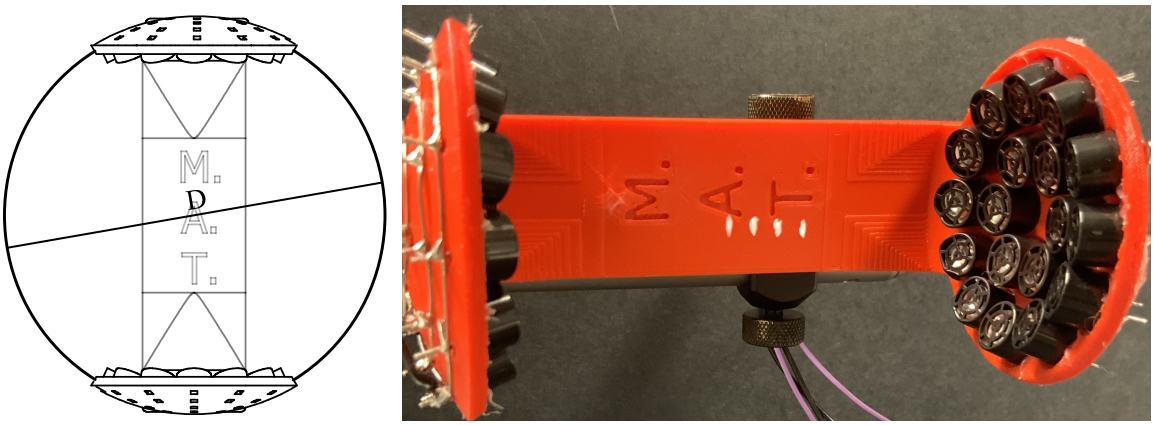

(a) (b)

Figure 3.3: AL design and demo. (a) The AL consists of two circular arrays of 18 transducers located on the inner surface of an imaginary sphere, the diameter of the sphere is designed to be a multiple of an acoustic half-wavelength. (b) Four white styrofoam particles are acoustically levitated in the central nodes of the AL field.

to levitate [12]. Nevertheless, it was found that the field can still be detected at lower power than the required for acoustic levitation, which is enough to measure acoustic forces on a microscopic particle. Thus only a function generator (TTi TG120) is used to directly feed both transducer arrays of the AL.

The input signals applied during the experiments reported here are sinusoidal waves with a frequency[3] of $39.4 \pm 0.3\,\mathrm{kHz}$ and peak-to-peak amplitudes ranging up to $6\,\mathrm{V}$. A single signal is used to feed all the transducers simultaneously.

[3]The frequency was selected empirically by doing a quick scan around the centre frequency of the transducers and looking for the most stable levitation of styrofoam particles.

3.2 Measurements

The dynamical response of the optically levitated particles is studied by tracking their position (x, y) and the intensity of scattered light (I) with the PSD, as explained below. The input peak-to-peak amplitude (A_{pp}) and the position (ALx, ALy, ALz) of the AL are used as degrees of freedom. ALy moves the levitator along the direction of the trapping laser beam while ALx and ALz move it along the horizontal plane, perpendicular to the beam.

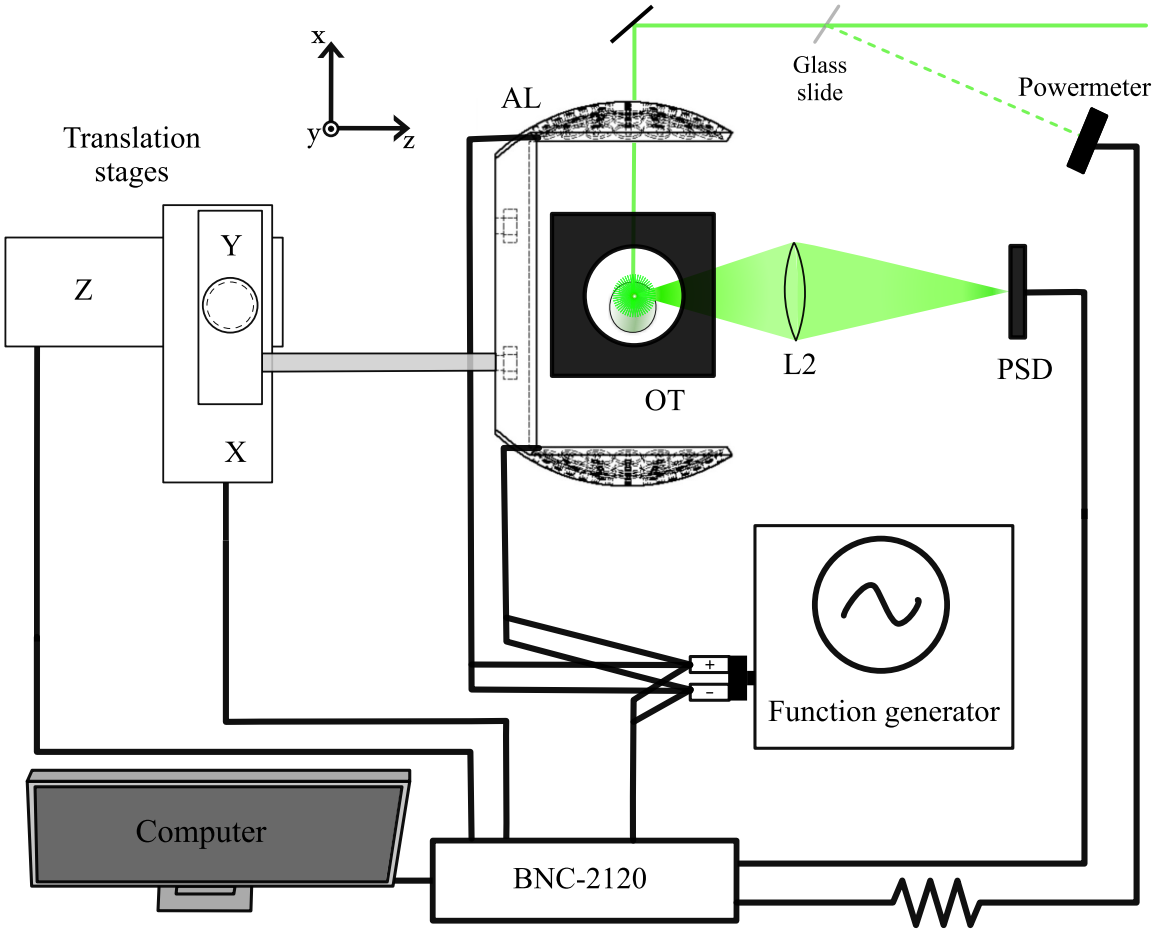

Figure 3.4: Top-view diagram of the setup with electronic connections. The intensity of scattered light (I) and motion (x, y) of the trapped particle are measured through the PSD. The function generator is used to control the amplitude (A_{pp}) and frequency of the AL input signal. The position of the AL (ALx, ALy, ALz) is controlled with translation stages. A thin glass slide is used to split a small percentage of the laser into a powermeter, used to record fluctuations in the laser power (P). All the variables are simultaneously collected in the BNC-2120 terminal.

Figure 3.4 shows the electronic connections in the experimental setup. Each measuring instrument (except the manual stage for the ALy position) is connected to a BNC terminal block (National Instruments BNC-2120). All the variables are recorded and monitored in real time with a LabView program, employing sampling frequencies of 0.1-1.0 kHz. The A_{pp} variable is computed within the LabView program from the voltage data obtained directly from the power source. Finally, the data is analyzed using Python and MATLAB.

3.2.1 Position sensing

Optically levitated particles scatter the trapping laser light in all directions. The aspheric planoconvex lens L2 ($f = 50$ mm) is set outside the optical cage to focus a portion of this scattered light. The 2D sensor of the PSD is placed at the image plane of the particle, where the light focuses onto a light spot (see Fig. 3.5). The following paragraphs offer a brief explanation of how the PSD records this light spot's intensity (I) and position within the sensor (X, Y) and how the motion of the actual particle is subsequently obtained.

PSDs are devices that use the *lateral photovoltaic effect* to track the position of a light spot on their semiconducting sensor. The PSD used here (Thorlabs PDP90A) has a two-dimensional tetra-lateral silicon sensor with one electrode on each of its four corners. When a light spot is generated on its surface, a photocurrent is produced, inducing output currents I_A, I_B, I_C and I_D, respectively, on each electrode. The detector then outputs three channels computed by the following expressions [55]:

$$\begin{aligned} I_X &= (I_A + I_D) - (I_B + I_C)\,, \\ I_Y &= (I_A + I_B) - (I_C + I_D)\,, \\ I &= I_A + I_B + I_C + I_D\,. \end{aligned} \tag{3.1}$$

Equation (3.1) gives a measure of the light intensity received by the sensor, while the position of the light spot within the PSD sensor ($\mathbf{r}_{PSD} = (X, Y)$) is calculated by

$$X = L\,\frac{I_X}{I}\,, \tag{3.2}$$

$$Y = L\,\frac{I_Y}{I}\,, \tag{3.3}$$

where $L = 5$ mm is half the width of the sensor. If the light spot is at the centre of the sensor, then $X = Y = 0$ mm, and if it is, for example, at the top right corner, then $X = Y = 5$ mm.

The magnification of the optical system shown in Fig. 3.5 is given by

$$M = -\frac{b}{a}\,.$$

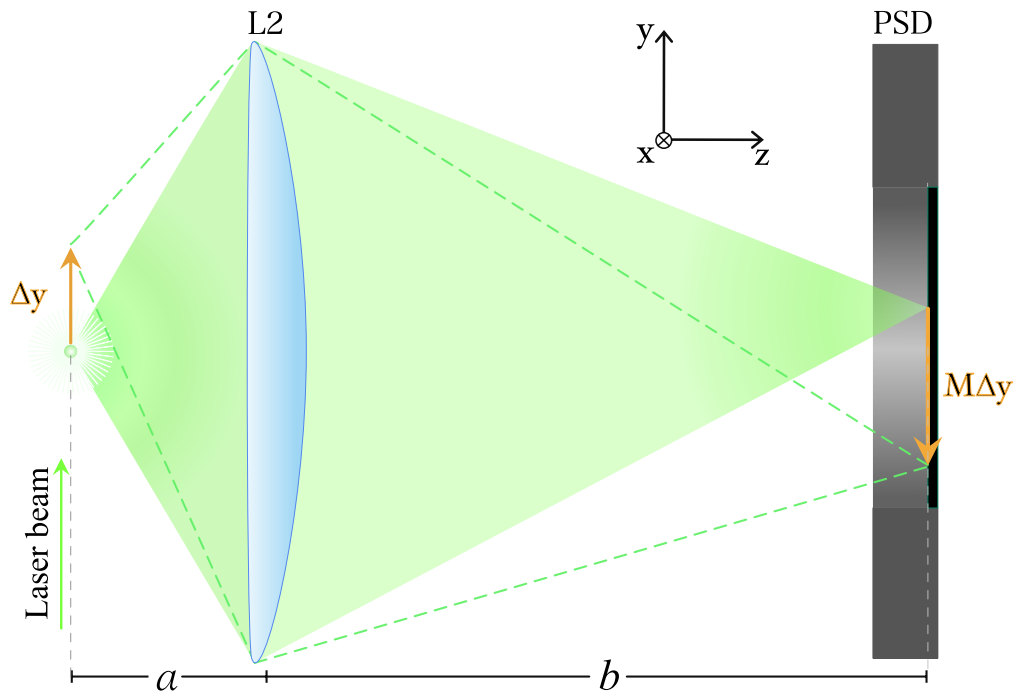

Figure 3.5: Diagram of the imaging system used to record the particle's motion. The lens L2 is at a distance a from the levitated particle to create a magnified image of it on the PSD sensor, located a distance b from L2. When the particle moves, the light spot on the PSD shows a correspondingly magnified displacement.

Since the focal length of the lens (f) is known, it suffices to measure b and use the thin lens equation to calculate the magnification as:

$$M = \frac{f - b}{f} \,. \tag{3.4}$$

Hence the real displacement of the levitated particles is calculated, using Eqs. (3.2) to (3.4), as:

$$\mathbf{r} := (x, y) = \frac{\mathbf{r}_{PSD}}{M} \,. \tag{3.5}$$

Notice that the use of a projected image on a fixed 2D sensor only allows measuring motion in the xy-plane. However, in the present case, conclusions can be drawn for the z-dimension by considering the symmetries of the system, mainly the axial symmetry of the AL.

3.2.2 OT stiffness

The trapped micro-particles exhibit Brownian motion because of thermal equilibrium with the surrounding medium (air). This motion can be seen as high-frequency

noise in the x and y data, and the amplitude of this noise will depend on the trap stiffness. Thus, following the method proposed by [56], the trap stiffness information is extracted from this thermal motion.

Position distributions $\rho(x)$ and $\rho(y)$ are obtained by generating histograms of the thermal motion extracted from a short time period of the x and y data, during which the AL is turned off.

Boltzmann statistics states that the probability distribution ($\rho(\mathbf{r})$) of finding a molecule or small particle under a potential $U(\mathbf{r})$ in a volume $d\mathbf{r}$ during thermal equilibrium is given by

$$\rho(\mathbf{r})d\mathbf{r} = Ce^{-\frac{U(\mathbf{r})}{k_B T}}\,, \tag{3.6}$$

where C is a normalisation constant, T is the temperature of the system and k_B is Boltzmann's constant. Thus the potential experienced by the particle is obtained by measuring ρ and solving for U in Eq. (3.6):

$$U(\mathbf{r}) = -k_B T \ln(\rho) + k_B T \ln C\,. \tag{3.7}$$

The last term is a constant potential offset and thus can be neglected.

Applying Eq. (3.7) on $\rho(x)$ and $\rho(y)$ gives potential profiles in both dimensions. Finally, these potentials are fitted with a quadratic curve to approximate a harmonic trapping potential and obtain the trap stiffness as with Eq. (2.4).

3.2.3 Acoustic force

The AL force can be measured as an external force acting on the optically trapped particle, using the information of the particle's position ($\mathbf{r}$) and the trap stiffness (κ). Equation (2.3) is used to describe the optical-trapping force ($\mathbf{F}_{OT}$) as a harmonic force exerted on the particle. If the particle stays displaced from its equilibrium position, it means an external force pulls the particle outward from the OT.

After successfully trapping a particle in the OT, the AL is turned on to study the acoustic field's effects on the particle. Initially, the most evident effect is the appearance of long position fluctuations of the order of 10 s in the y data, as a response to increments in A_{pp} (see Fig. 4.2(a)). These fluctuations make it hard to quantify a displacement from the equilibrium position. Hence, long-time averages are taken to obtain more reliable measurements. Given a fixed condition in ALx, ALy, ALz and A_{pp}, the average position is taken from an approximately 2 min long batch of data.

Thereby assuming that the particle is in mechanical equilibrium under the optical and acoustic fields, we measure the acoustic force as per the following expression:

$$\mathbf{F} = -\mathbf{F}_{OT} = \kappa(\langle\mathbf{r}\rangle - \mathbf{r}_0)\,, \tag{3.8}$$

where $\mathbf{r_0}$ is the equilibrium position of the particle in the OT, and the angle brackets around $\mathbf{r}$ denote averaging over time.

4 Results and discussion

This chapter presents and discusses the measured stiffnesses of the OT and the resulting measurements of the acoustic force field, performed with optically levitated probe particles, culminating with a force map along the AL axis in Section 4.3. Additionally, Section 4.4 presents some interesting observations about the angular dynamics of the levitated particles, along with consequent results.

4.1 OT stiffness

The process of measuring the trap stiffness for one levitated particle is summarized in Fig. 4.1 for the radial (x) and axial (y) directions of the laser beam. First, the thermal motion of the particle is shown in Figs. 4.1(a) and 4.1(d). This thermal motion is obtained by applying a high-pass filter (Butterworth, order 1, critical freq. 3 Hz) to the motion data x, y (measured as with Eq. (3.5)) from a period of about 10 s in which the AL was off[1]. The filtering is applied in order to neglect slow fluctuations generated by air currents or variations in the laser power.

Making position histograms (Figs. 4.1(b) and 4.1(e)) from the thermal motion yields the respective probability distributions. Then, applying Eq. (3.7) (with $T = 293.0\,\mathrm{K}$) gives the potential energy profiles plotted in Figs. 4.1(c) and 4.1(f).

Equation (2.4) is used to fit the potential wells, giving the following radial and axial stiffnesses:

$$\kappa_x = 19.7 \pm 0.80\,\mathrm{nN/m}\,,$$
$$\kappa_y = 2.56 \pm 0.127\,\mathrm{nN/m}\,.$$

Here, the data acquisition rate is of 200 Hz and the magnification of the optical system $M = -3.84$.

As expected, κ_x is larger than κ_y. This reflects the fact that trapped particles have more freedom to move in the y-direction than in the x-direction within the OT, as can be noticed in results of the following sections.

[1] This data is taken from the initial control data of the experiment discussed in Section 4.3

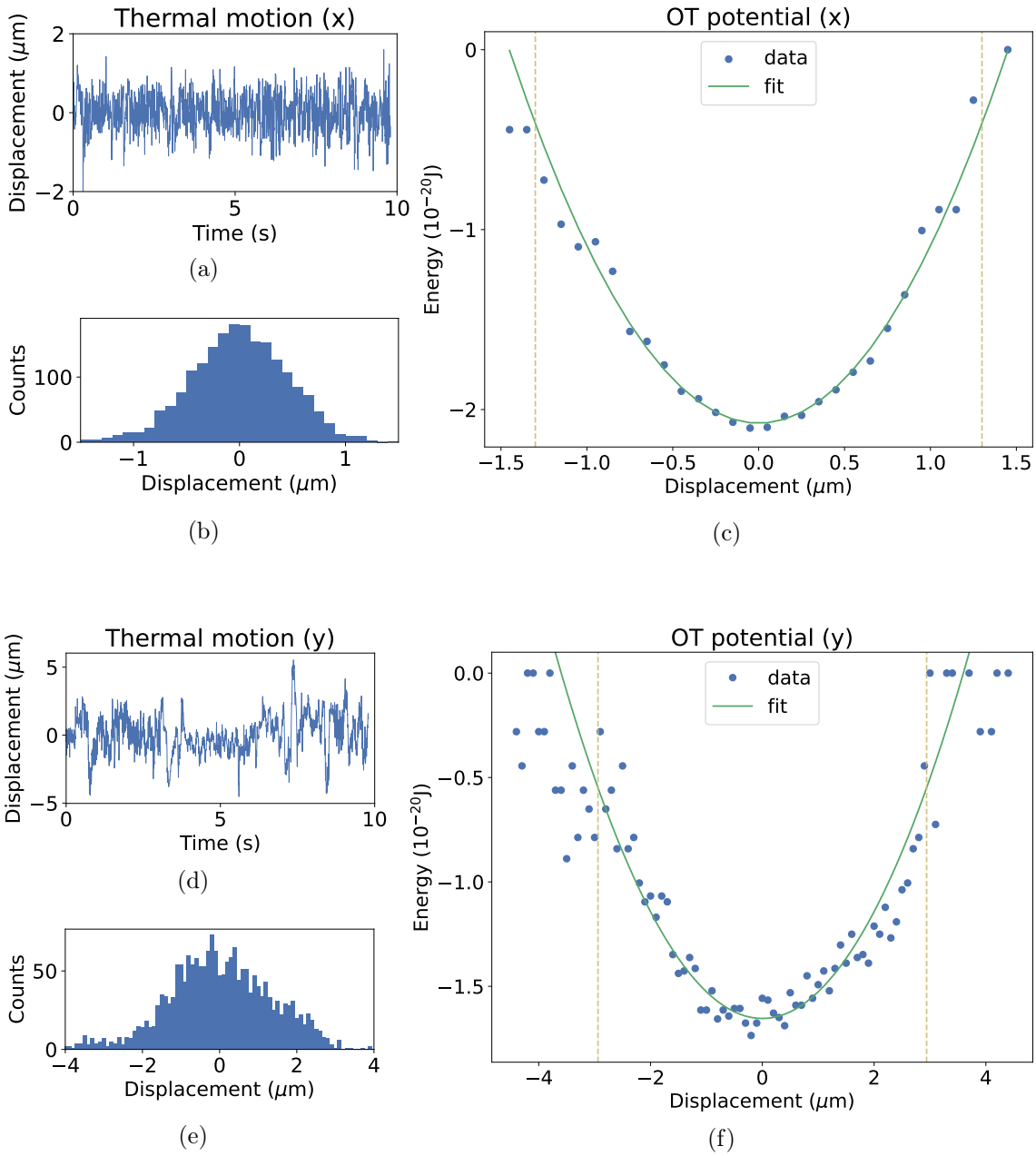

Figure 4.1: Obtaining the OT stiffness in x (top) and y (bottom). (a) and (d): Thermal motion obtained after applying a high-pass filter to the motion data of the levitated particle. From it, histograms (b) and (e) are obtained, respectively. Finally, potential wells (c) and (f) are plotted by applying Eq. (3.7) to (b) and (e), respectively. The green parabola is fitted to the x (y) potential using the 26 (59) points closer to the centre, delimited by the dashed vertical lines.

4.2 Response of the trapped particle to the AL field

Figure 4.2 shows the response of a particle's position to increments in the AL input amplitude (A_{pp}). By the end of the measurement, the particle reaches a condition where the optical forces can no longer pull it back to the equilibrium position, and it breaks out of the OT. A quadratic response is observed in both x and y. Notice that y-displacements are about two orders of magnitude larger in scale than x-displacements.

The plot of Fig. 4.2(a) shows the highest critical $A_{pp} = 6.27\,\mathrm{V}$ achieved before losing a particle. Notice that the left vertical axis is inverted to elucidate the correlation between the two graphs.

From the full motion data, batches of 100 s are selected between increments of A_{pp}. Each batch is taken from roughly the last 100 s before A_{pp} was modified or the particle was lost (last batch). This selection helps neglect possible inertial effects produced during the transient state of the particle jumping between stable positions. Average positions are taken from each batch and plotted in Figs. 4.2(b) and 4.2(c). That is to say that every data point in these plots has an average y or x position as vertical coordinate and an average A_{pp} as horizontal coordinate. The error bars in the plots correspond to standard deviations of the batches, which are related to position fluctuations.

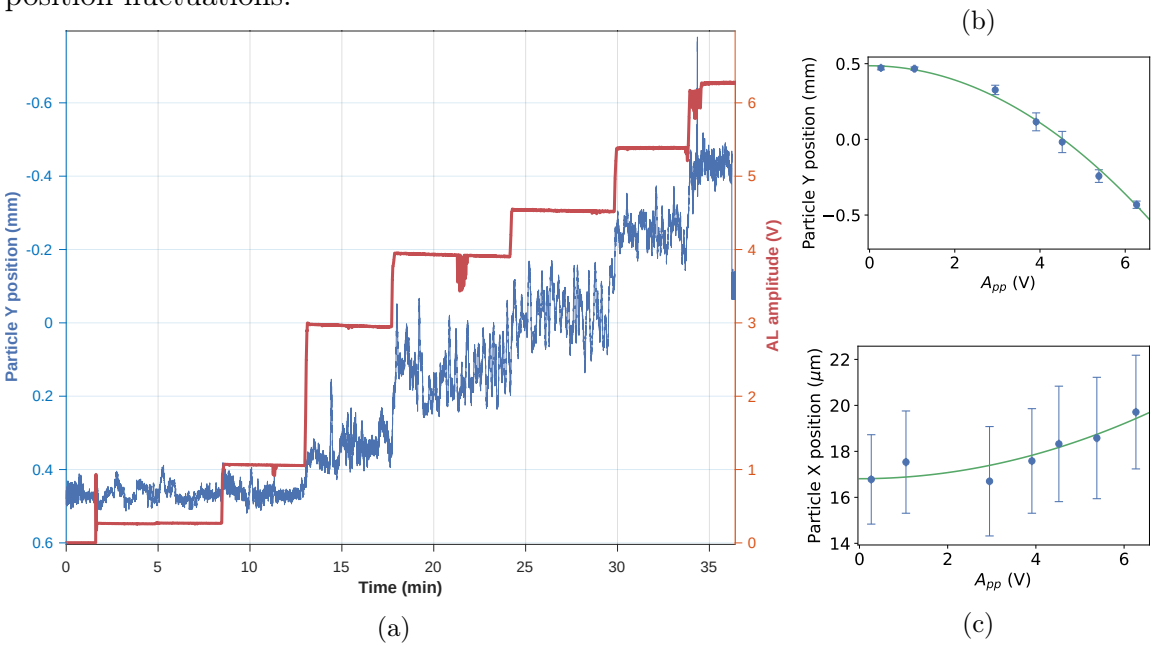

Figure 4.2: Kinematic response of an optically levitated particle to increments in the AL input amplitude (A_{pp}). (a) Particle's y data (blue) plotted together with the A_{pp} data (red). A_{pp} is manually incremented in steps until the particle gets knocked out of the OT. On the right, the average position is plotted as a function of A_{pp}. A quadratic response (green fits) is shown in both x (b) and y (c).

The AL position fixed during this measurement is such that the particle levitates near the AL centre within a 0.5 cm precision. The data acquisition rate is 1000 Hz, and

the optical magnification $M = -4.08$.

In the red A_{pp} plot some data "bumps" can be seen around $t = 11, 22, 34$ min. These bumps should be ignored since they emerge in computation as an effect of the difference between the data acquisition rate and the actual signal frequency.

Discussion

The changes in position shown in Fig. 4.2 are clear evidence that the AL exerts a force $\mathbf{F}$ on the optically levitated particle, which increases monotonically with A_{pp}. The quadratic response found in Figs. 4.2(b) and 4.2(c) yields the relation with the acoustic force $\mathbf{F} \propto A_{pp}^2$. This quadratic behaviour is in agreement with Eq. (2.12), given that A_{pp} is proportional to the acoustic pressure amplitude produced by a transducer. The same conclusion was similarly encountered by Ritsch-Marte et al. [37, 38], although with a non-focused acoustic field in a microfluidic medium.

Another way to visualize the motion of the particle throughout the experiment is shown in Fig. 4.3. It becomes clear how increasing A_{pp} pulls the particle down and slightly to the right, towards where one of the central pressure nodes is located. Unfortunately, the poor calibration of the particle position relative to the AL centre prevents confirming which of the two central nodes is involved since the experiment was performed before obtaining the mappings presented in next section.

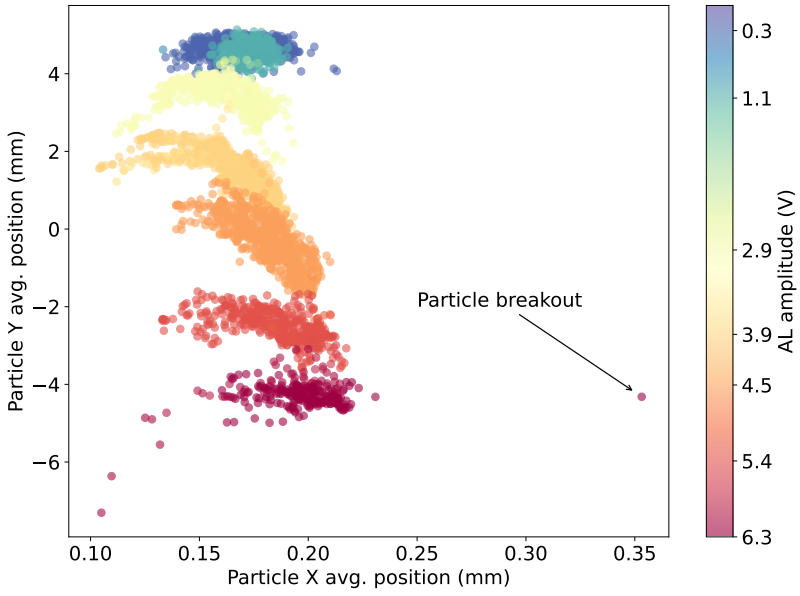

Figure 4.3: 2D average motion of the trapped particle. Particle position averaged every 0.5 s is plotted and color is used to indicate the amplitude of the feeding signal.

A further step for this experiment would be to repeat it in well-known positions around and within one of the nodes or antinodes.

4.3 Map of the acoustic field

Figure 4.4 exhibits the mapping of the acoustic force field $\mathbf{F} = (F_x, F_y, F_z)$ along its symmetry axis. The field is probed with an optically levitated particle and measured as explained in Section 3.2.3, obtaining forces on the scale of 100 fN. The scanning is performed by moving the levitator along the x-direction (ALx) in steps of 0.4 mm, so the particle probes across three of the central nodes. The system is aligned to keep the particle at the AL axis throughout the scanning by properly fixing ALy and ALz. The input voltage is fixed at $A_{pp} = 2.8\,\mathrm{V}$.

The data is divided into batches of 130 s from which the average positions are calculated. As in the previous section, the error bars are standard deviations of the batches and result from position fluctuations. Two control data points (red) are taken with the AL turned off at the beginning and end of the experiment. These define the equilibrium position of the OT ($\mathbf{r}_0$ in Eq. (3.8)).

Figure 4.4(a) shows the map of the x component of $\mathbf{F}$, which reveals a clear sinusoidal profile. A sine function is fitted, and with it, the pressure nodes (green circles) and antinodes (yellow circles) are plotted by comparison with Fig. 2.4.

The force map along the y-direction (Fig. 4.4(b)) does not unveil any clear attribute expected from the acoustic levitation field. This suggests that the radial acoustic force is negligible because of symmetries at the axis. Furthermore, a correlation is found between F_y and the laser power level during the experiment (read the discussion below). This correlation is evidence that the particle is indeed on the AL axis, at least in the y dimension, since it shows that other effects have a more significant impact on the particle y-motion than the acoustic field.

To compensate for the poor experimental calibration of the particle's position relative to the AL, we use the knowledge that an antinode exists at the very centre of the AL to locate the centre of the field on the force maps (purple vertical line). Given that the AL consists of two symmetric arrays of transducers emitting all in-phase is fair to approximate the field at the axis by a standing plane wave. Look at Eq. (2.8) to verify that there is an antinode in the centre ($x = 0$) of a standing wave field, given that both travelling waves are emitted in phase. This fact has also been confirmed with visualizations of the field [28].

In order to better visualize the $\mathbf{F}$ field, the force maps are plotted in a reference frame where the AL remains static, and the particle moves through the field. Hence, according to the plots, the experiment is run from right to left.

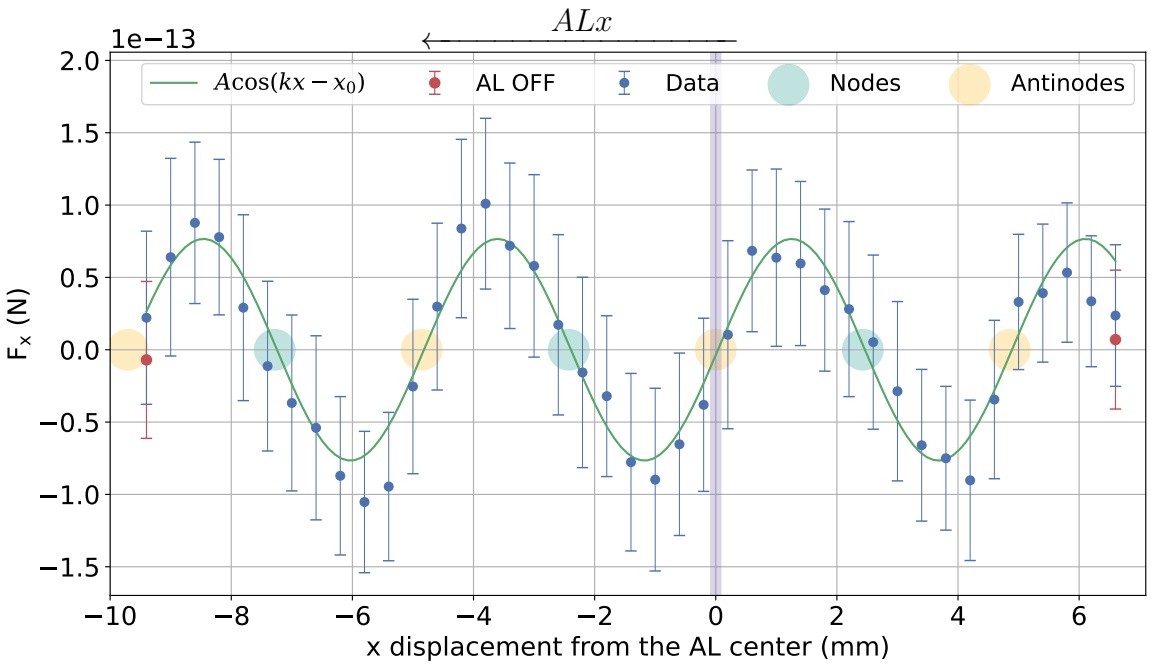

(a)

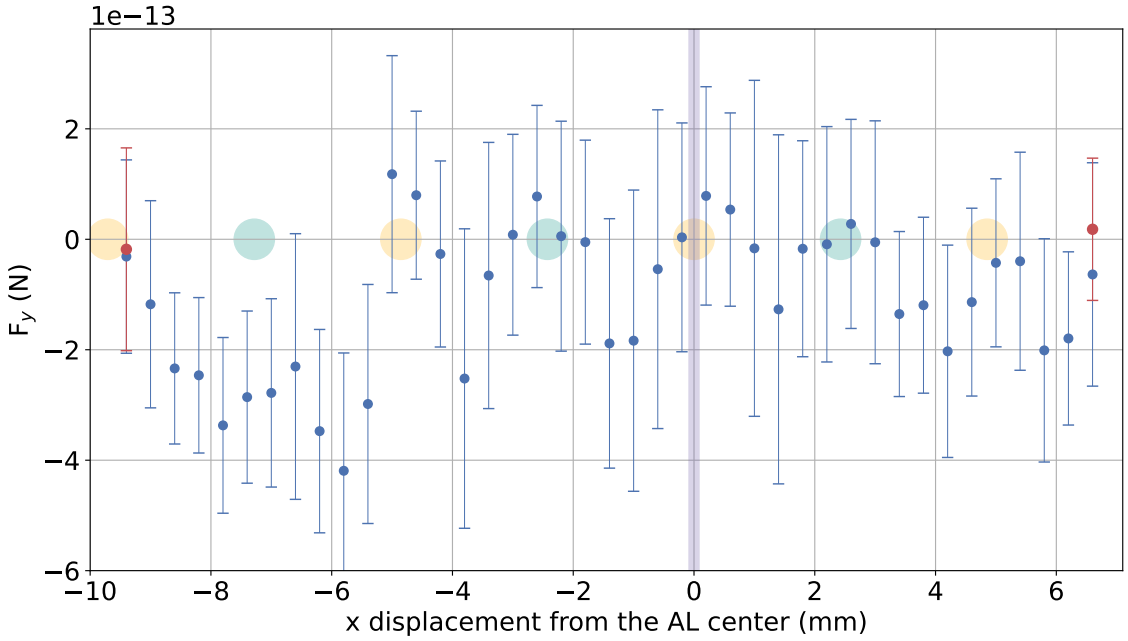

(b)

Figure 4.4: Mapping the acoustic force **F** exerted by the AL on an optically levitated silica microparticle. The x (a) and y (b) components are plotted separately. Both maps come from the same scan along the symmetry axis. A siusoidal function (green curve, $A = [7.66 \pm 0.44] \times 10^{-14}$, $k = 1.29 \pm 0.013$) is fitted to F_x, and with it, the pressure nodes (green circles) and antinodes (yellow circles) are found. Control measurements with the AL turned off are plotted in red. The centre of the field is marked with a vertical purple line.

Discussion

The force maps obtained show the expected behaviour of an acoustic standing wave trap through its axis. Since there is a cylindrical symmetry in the field, it is expected that the radial components of $\mathbf{F}$ (F_y and F_z) cancel at the axis. Hence the behaviour at the axis is similar to that of a plane wave, where only F_x is significant and has a sinusoidal behaviour (see Eq. (2.8)). Unlike a plane standing wave, the real field should exhibit an amplitude increase towards the central point (upon which the transducers are focused) and a decrease towards the transducer arrays. However, this variation in amplitude is not a prominent feature of the graphs presented above. Longer or off-axis scans should be performed to observe that variation.

Given that the lower axial stiffness leads to larger error bars in the y component than in the x component, it is plausible to say that F_y becomes very small in Fig. 4.4(b), as expected at the axis. However, the left side of the plot contains a particular data segment that does not overlap with a null force value. One possible explanation for this is revealed by the table below, which shows a significant correlation of F_y with the laser power level (P) compared to other variables.

Correlation of F_y with:	
F_x	0.300
P	0.689
A_{pp}	-0.168

Table 4.1: Correlation of the vertical component of the acoustic force (F_y) with other variables. A significant correlation is found with the laser power(P).

This is evidence that any radial acoustic force (expected to behave somewhat similar to F_x) is outweighed particularly by the effect of laser power fluctuations, which imply fluctuations in the scattering force of the OT. This finding adds to confirm the cancellation of F_y, and hence the particle being at the axis. Furthermore, it has been observed that scanning off-axis produces periodic peaks and valleys on F_y too, which is not the case here.

Figure 4.5 shows the plot of the P data (measured as shown in Fig. 3.4) normalized and divided into batches, the same way as the as the other data in this section. This plot features a power drop around the -6 mark of the horizontal axis, which can help to explain the F_y deviations from zero mentioned above.

With the parameters obtained from the sinusoidal fit on F_x and by recalling that the pressure-wave wavelength is twice the separation between nodes (Fig. 2.4), a wavelength value of $\lambda_{exp} = 9.71 \pm 0.097\,\mathrm{mm}$ is predicted. The actual wavelength of ultrasound at the experimental frequency is

$$\lambda = \frac{c}{\nu} = \frac{344.5\,\mathrm{m}s^{-1}}{39.4\,\mathrm{kHz}} = 8.744\,\mathrm{mm}\ ,$$

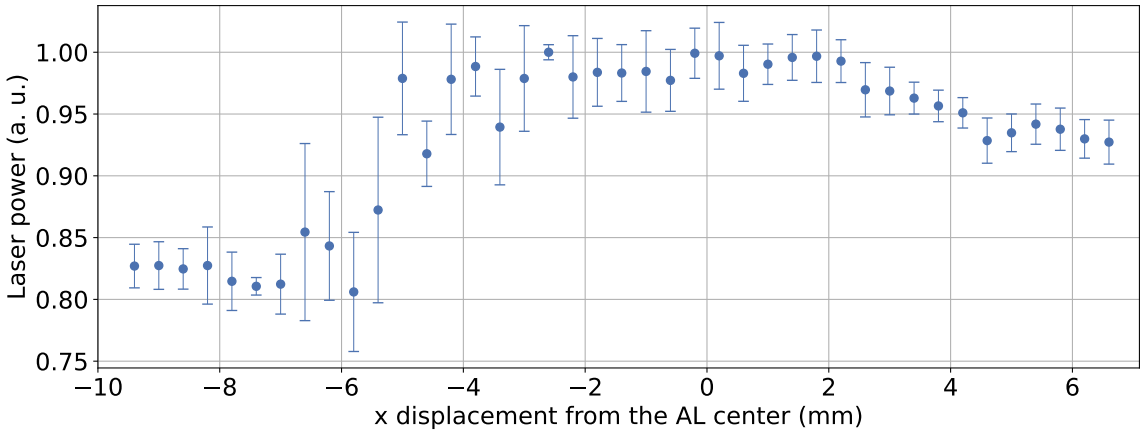

Figure 4.5: Laser power behaviour during the scanning of Fig. 4.4 ploted with the same horizontal axis.

where the speed of sound is taken at 22 °C in dry air. Hence λ_{exp} has an 11% error. A possible explanation is that the separation between nodes produced by a focused array of transducers like the one used here is not precisely $\lambda/2$, as it is for a simple standing wave [57].

More complete models could be used to fit the F_x map, but since the error bars are so significant, selecting which model fits better would become meaningless. The fluctuations that produced these big uncertainties on the plots could partly result from the lack of better air current isolation but also significantly from the intrinsic instabilities of the AL field. These instabilities partially come from the use of imperfect transducers, which introduce some degree of phase difference among them. However, even when using a single emitter, getting rid of the instabilities is not a trivial problem [58]. Moreover, the interference of other objects in the system, most prominently the optical cage, can introduce more reflections and deformations to the acoustic field increasing the instabilities.

It should be mentioned that with the current setup, performing full scans like the one presented in this section is somewhat cumbersome. Due to the system's sensitivity to air currents, any sudden movement in the lab can result in kicking the particle out of the OT. Adding the long time required for one measurement makes completing a scan with a single particle challenging. Hence, designing a better isolation setup for the system will improve the method's performance. Besides, scans carried at higher A_{pp} resulted in the particles being pulled out of the OT more often. All this should be easier to test and explore after using the maps to calibrate the position and acquire more knowledge of the field.

4.4 Angular dynamics

While conducting experiments with the OT, interesting observations were made about the far-field diffraction pattern of the levitated particles, projected in all directions onto the setup walls (see Fig. 2.3). Apart from the main bright and dark fringes produced by interference, some seemingly random spatial intensity fluctuations (SIFs) are often observed within the pattern. These fluctuations are seen as shadows and bright zones with the naked eye and are hypothesized to come from material inhomogeneities in the levitated particles. Attention is put on the SIFs because they exhibit horizontal rotations and oscillations through the setup walls. SIFs on both the side fringes and the diffraction rings on top show angular dynamics, most likely caused by the rotation of the levitated particle itself.

The photos on the right side of Fig. 4.6 are frames from a video in which some very distinguishable SIFs pass through a screen. To record such video, the PSD is removed from the setup to set the screen and film the portion of the diffraction pattern projected onto it with lens L2. Notice that when the highlighted SIF reappears on the screen, it has completed a $\sim 360^\circ$ track around the setup, and more than 2 s have elapsed. The left side of the figure illustrates how the particle's rotation is likely related to the periodic passing of SIFs through the screen. It is worth mentioning that the pattern rotations were always perceived to be horizontal, namely with a vertical axis of rotation (parallel to the trapping laser beam).

When the PSD is being used to record the motion of the particle, it can likewise be used to record the scattering intensity (I) passing through the lens L2. Thus, if some bright SIF passes through L2, it should be recognizable as a peak in the I data. Likewise, a dark SIF creates a valley in I. Moreover, these peaks or valleys appear periodically if the particle rotates. This process is also portrayed in Fig. 4.6.

In practice, the amount of scattered light collected in the PSD may depend on factors other than the particle's rotations, like laser power fluctuations or varying reflections that produce noise. On top of that, the presence of both bright and dark SIFs within the same region of the pattern may cause the corresponding data peaks and valleys to average each other out. Hence it is usually not straightforward to pinpoint these periodic peaks or valleys in the I data. However, several tests (see Appendix A) qualitatively showed the expected periodicity in the I data when angular dynamics are observed through the diffraction patterns.

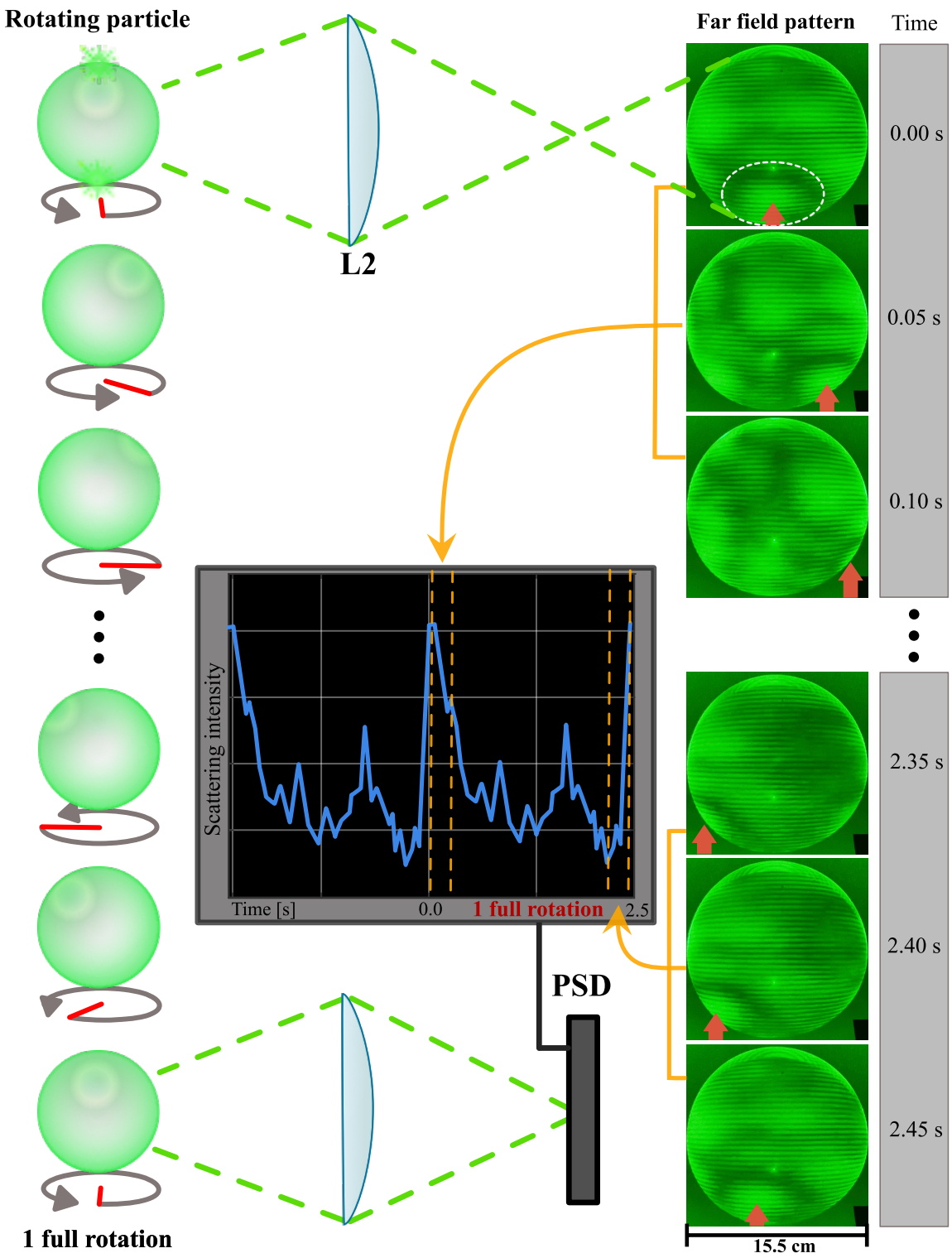

Figure 4.6: Measurement of a particle's rotation through its interference pattern. A sequence of selected frames from a video is shown on the right side. The photos show the far-field diffraction pattern of the particle, projected with lens L2 onto a screen. The left column illustrates how the passing of some spatial intensity fluctuations (SIFs) through the screen is related to the rotation of an optically levitated particle. Notice that this illustration exaggerates the angular steps between frames. In this particular case the period of rotation is $\sim 2.5\,\mathrm{s}$. If a PSD is used to measure the scattering intensity, the passing of some SIFs can be identified as peaks or valleys, resulting in certain periodicity on the data.

AL effect on rotations

The diffraction pattern produced by particles in the OT can show rotations even when the AL is off. However, an evident dependency of the rotation speed on the acoustic field amplitude and position has been observed. The angular frequency (ν) of the above-mentioned rotations can be increased and decreased by manipulating A_{pp} (graph shown in Appendix Fig. A.3). Since the AL field provides only mechanical perturbations to the particles, this dependency is evidence that the angular dynamics exhibited by the patterns indeed come from the particle's angular dynamics. Hence ν must be related to the angular frequency of the particle rotations. All the observations above motivated an analysis of the scattering intensity channel (I) of the experiments reported in the previous sections of this chapter, with the purpose of studying ν.

Following the analysis of sections 4.2 and 4.3, the I data has been respectively divided into batches. To systematically obtain a ν value, the *power spectral density* of each batch is computed, and the first prominent spike in the frequency spectrum is selected (see Appendix B).

Figure 4.7 shows the response of ν to increments in A_{pp}, during the experiment of Section 4.2. The rotation frequency exhibits a rapid increase with A_{pp}, for which a power law is fitted.

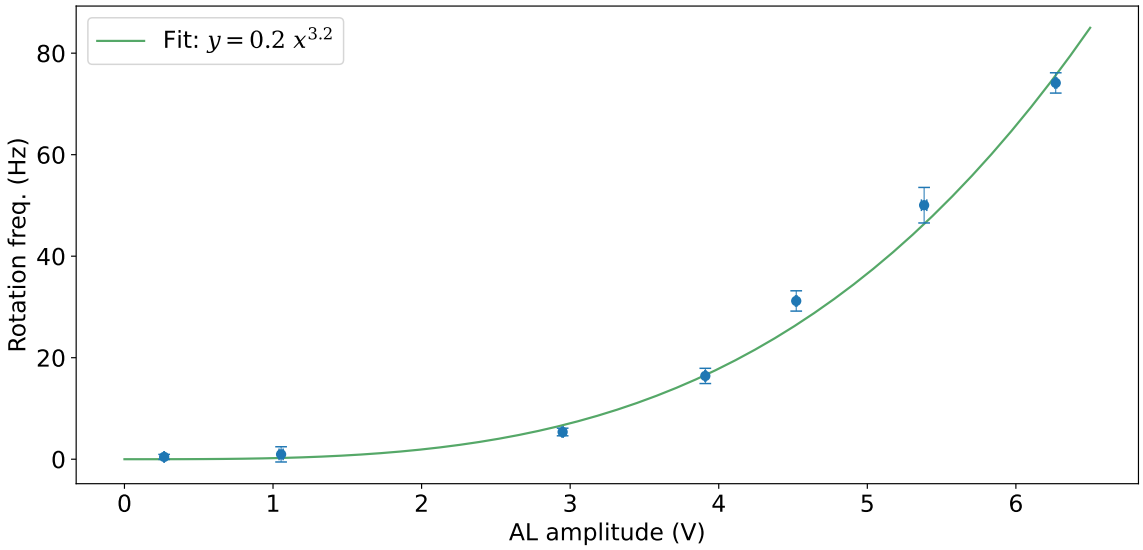

Figure 4.7: The rotation frequency of an optically levitated particle increases as a response to increments in the amplitude of the AL field. A power law is fitted.

Figure 4.8 shows the response of ν throughout the scan of Section 4.3. The nodes and antinodes are plotted as in Fig. 4.4 for reference. This plot can be interpreted as a map of the magnitude of torques applied by the AL field to the levitated particle. A correlation with the force maps is not evident. However, there is a seeming tendency of ν to have local minima (i.e. the rotations stop) within the antinodes, and local maxima (i.e. maximum rotation speed) near the nodes. A different frequency

behaviour can be identified at the right end of the plot, which might be explained by recalling that the initial condition (red data point) involves the AL turned off and no rotations.

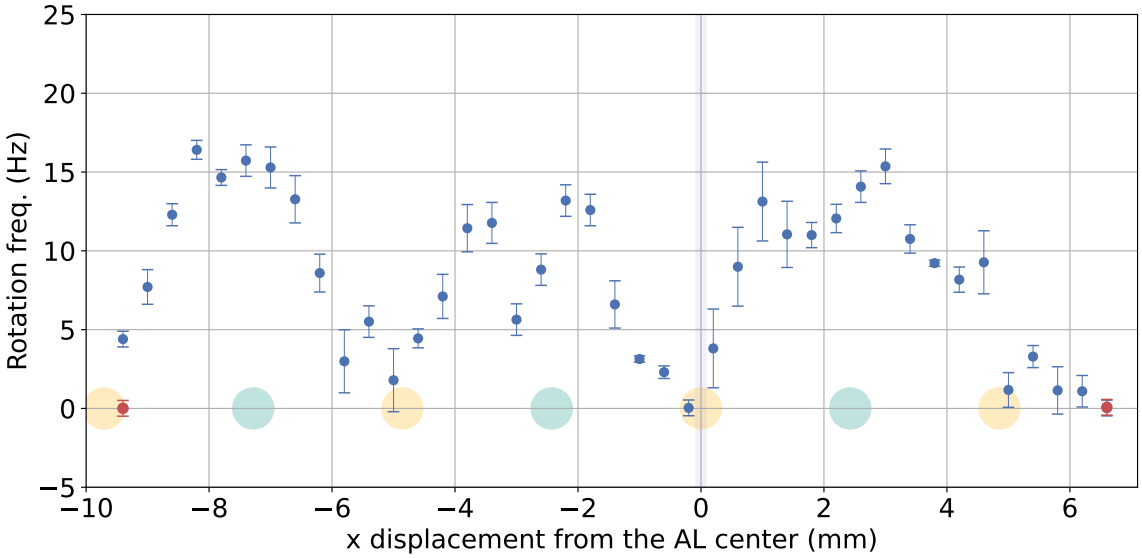

Figure 4.8: The rotation frequency of an optically levitated particle varies with its position relative to the AL. As before, the green and yellow circles represent nodes and antinodes, respectively.

Something that is not possible to analyze with the methods used here is the direction of rotation of the particles. It would be very interesting to analyze this since it has been empirically observed that the rotations can change directions during experiments.

5 Conclusions and outlook

An optical levitation trap has been built and used to measure an acoustic levitation force field. The remarkable sensitivity of this system allows measuring acoustic forces down to the scale of 1×10^{-13} newtons. Scanning along the acoustic levitator's axis, a force mapping has been produced for both an axial and a radial component. The axial component coincides qualitatively with the expected profile of a standing wave field, which allows locating the nodes, antinodes and the centre of the field. The radial component shows negligible force, as expected at the axis, due to the symmetry of the field. It is also shown that the force increases quadratically with the input amplitude of the AL, which agrees with Gor'kov's theory and with existing literature on sono-optical systems. Additionally, it has been observed that the acoustic field affects the angular dynamics of the optically levitated particles, inducing torques that depend on the levitator's input amplitude and position.

The force map presented in Section 4.3 should help to precisely calibrate the particle position relative to the acoustic field itself. A position calibration will allow deeper and more efficient exploration of the field using the same methods. Particularly one can study the forces within the nodes and antinodes after knowing their exact location. Moreover, scan routines can be programmed to obtain 2D or 3D maps, as in [59].

Due to the difference between axial and radial stiffnesses, the force measuring method presented has a greater resolution in the x-direction than in the y-direction. This could be improved, for example, by using a counterpropagating optical trap.

Another essential step to improve the method is to enhance the air current isolation of the system, perhaps by designing a big cage that isolates the whole AL and OT simultaneously and allows taking the optical cage away. Moreover, different acoustic levitator designs could be studied without extensive setup modifications.

Further studies should be performed to better understand the effect of the acoustic field on the rotational dynamics of the spherical levitated particles. However, the use of standing-wave acoustic levitators could emerge as a simple method to produce torques on small levitated objects for many potential applications. For example, one could study the collision dynamics of two rotating micro-droplets.

As far as my best knowledge goes, the combination of acoustic and optical trapping setups in gaseous media has not been reported before. Hence, this work could serve as a first step into sono-optics in air, which could lead to the development of enhanced techniques for characterizing fields or handling particles in acoustic levitation. For

example, I anticipate that by using a similar setup to the one described here and drawing from the knowledge of a field map like the one obtained, micrometric and sub-micrometric particles may be optically placed in the trapping point of an acoustic field very accurately. Additionally, this would allow for the particles to be positioned without using handling tools that disturb the field, which could be a significant factor in pushing down the size limit of acoustically levitated particles. Conversely, one could use the acoustic field to do a rough trapping of a particle and the OT to trap it more sharply, even with particles that would usually be too big for optical trapping. In this sense, with the help of an acoustic field, the laser power needed for optical trapping might be reduced. Furthermore, combined sono-optic effects could be used to control the orientation of levitated objects, leading to contactless placement techniques with potential industrial applications.

A Angular dynamics tests

Some tests have been run to observe the response in the scattering intensity data (I), hypothesized to show periodic peaks as an effect of the particle's rotations, to changes in the AL feeding amplitude (A_{pp}).

If there is a periodicity in I due to the particle's rotations, it should be possible to measure the rotation frequency as

$$\nu = \frac{1}{\Delta T} \tag{A.1}$$

where ΔT is the time separation between characteristic peaks or valleys in the data.

Empirical observations of the rotating diffraction patterns imply that ν increases and decreases rapidly with A_{pp}. Several tests where run to observe these response of the particle to different changes in the acoustic amplitude, by manually modifying A_{pp}. Figure A.1 shows ν and A_{pp} plotted aside for one of these tests that qualitatively show the expected response.

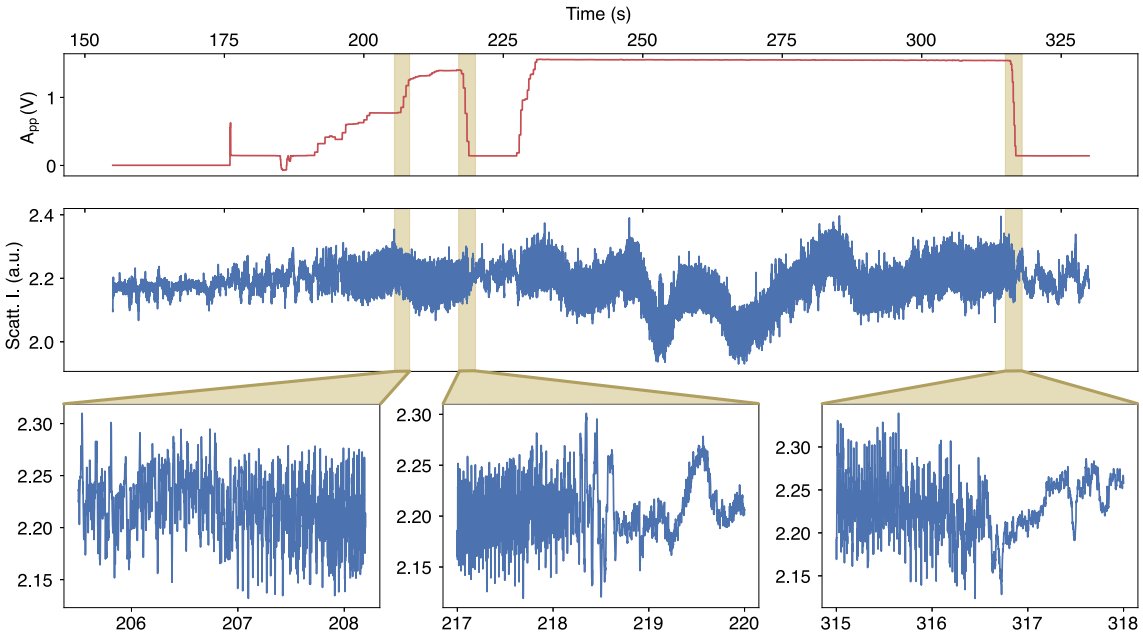

Figure A.1: Test data showing qualitative correlation between A_{pp} and ν. ν is interpreted as the frequency of high peaks appearing in the scattering intensity (I) data. Three windows are selected to show how the periodicity increases when A_{pp} is increased (left) and decreases when A_{pp} is decreased (centre and right).

It is easy to see that for lower values of A_{pp}, high peaks in I appear less frequently, but they appear very tight together for higher values of A_{pp}. The three selected windows at the bottom highlight how ν changes when A_{pp} increases or decreases rapidly.

Although the correlation can be seen, the overall behaviour of the I data makes it difficult to do a quantitative analysis. To do such an analysis, we use the data shown in Fig. A.2 from another test in which the PSD was getting saturated, causing I to reach a fixed maximum value. This makes it much easier to do a quantitative analysis of the period between consecutive maximum peaks. Peaks are found with Python's Scipy library to then compute the period ΔT between consecutive peaks. This procedure was not followed in the rest of the thesis because saturating the PSD is not desirable.

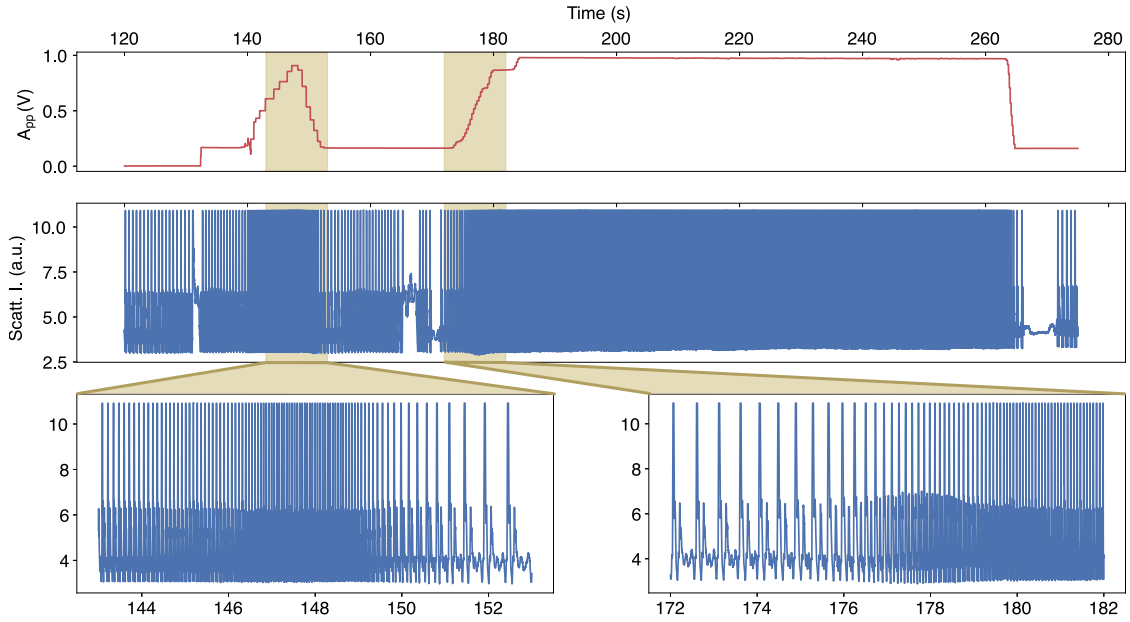

Figure A.2: A_{pp} and I data from a test during which the PSD gets saturated, making it easy to determine the peak frequency.

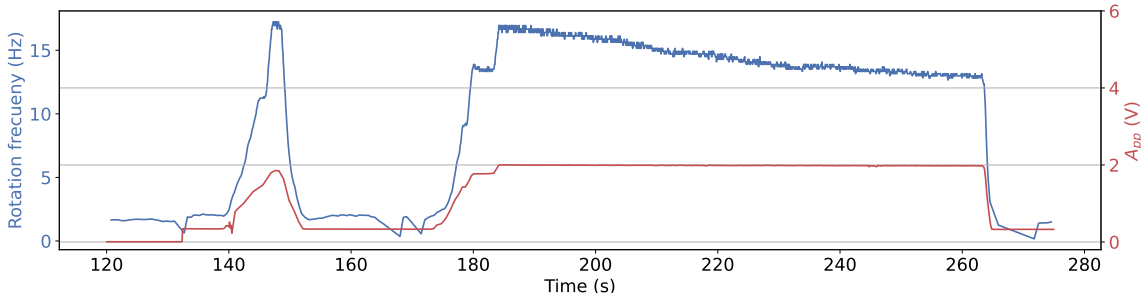

Figure A.3: Controlling a levitated particle's rotation frequency by manipulating an acoustic levitation field. The period between spikes in the scattering intensity data shown in Fig. A.2 is computed, and the inverse (the peak frequency) is plotted in blue. Plotting this together with the input amplitude of the acoustic levitator A_{pp} (red) reveals a clear correlation.

Figure A.3 shows a graph of the peak-frequency (ν, blue graph) computed from the data in Fig. A.2 as with Eq. (A.1). Plotting it together with the A_{pp} data (red graph) reveals that ν responds very sensitively to changes in A_{pp}, showing that ν can be

controlled by modifying A_{pp}. Nevertheless, a decay in ν can also be observed when A_{pp} is left constant for a long time.

All the analysis above coincides with the empiric real-time observation of the change in rotational speed of the far-field diffraction pattern through the laboratory walls.

B Frequency measurements

In order to measure the periodicity of the scattering intensity data (I), a procedure to compute the frequency spectrum of the data is desirable. In this case, the *power spectral density* is used, which is proportional to the square modulus of the Fourier transform. To do the computation, Matplotlib's `psd` function is applied to each desired batch of I data.

Figure B.1 shows examples of power spectral densities computed for different batches. Peaks in every spectrum are found with the Scypi library. After various examinations of the spectrum, the frequency corresponding to the first prominent spike in the data is manually selected as the fundamental frequency of the given batch. The frequency uncertainty is estimated by examining the width of the selected spike.

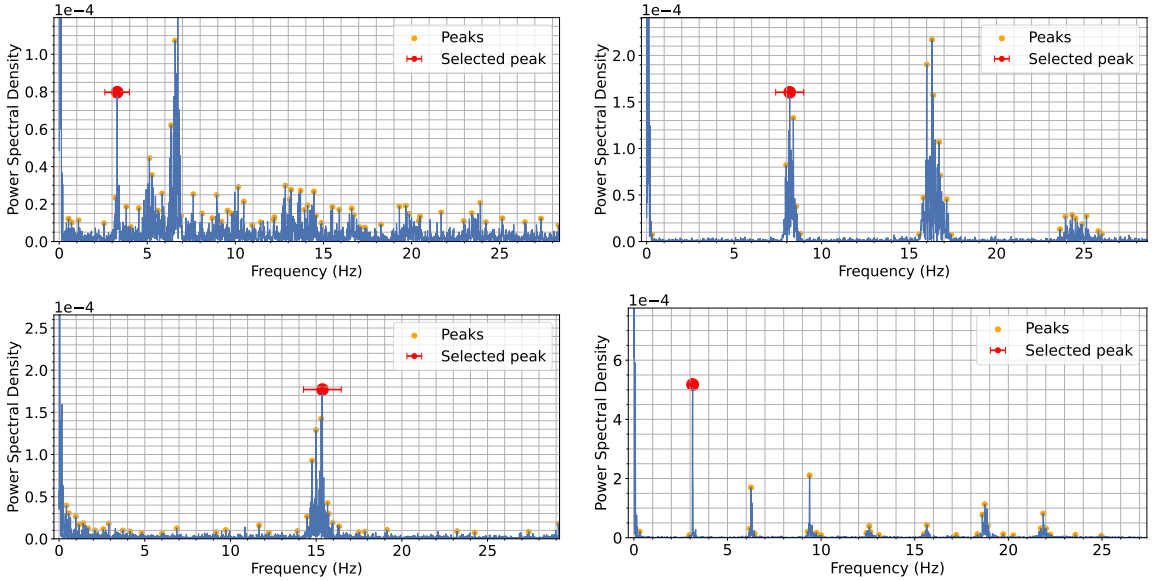

Figure B.1: Examples of power spectral densities computed for different batches of the scattering intensity data from the experiment of Section 4.3. After finding the peaks within each spectrum, a single one is selected as the fundamental frequency value of the batch.

References

[1]E. J. Davis, "A history of single aerosol particle levitation", Aerosol Science and Technology **26**, 212–254 (1997).

[2]E. H. Brandt, "Levitation in Physics", Science **243**, 349–355 (1989).

[3]E. Gibney and D. Fox, "Researchers create 3D display you can see, hear and feel", Nature, 10.1038/d41586-019-03508-1 (2019).

[4]R. Hirayama, D. Martinez Plasencia, N. Masuda, and S. Subramanian, "A volumetric display for visual, tactile and audio presentation using acoustic trapping", Nature **575**, 320–323 (2019).

[5]D. E. Smalley, E. Nygaard, K. Squire, J. Van Wagoner, J. Rasmussen, S. Gneiting, K. Qaderi, J. Goodsell, W. Rogers, M. Lindsey, K. Costner, A. Monk, M. Pearson, B. Haymore, and J. Peatross, "A photophoretic-trap volumetric display", Nature **553**, 486–490 (2018).

[6]Brigham Young University, *Beyond holograms: Star Wars-inspired 3D images float in free space, (2018)*, https://www.youtube.com/watch?v=1aAx2uWcENc, accessed 28/04/2022.

[7]A. Kundt, "Ueber eine neue Art akustischer Staubfiguren und über die Anwendung derselben zur Bestimmung der Schallgeschwindigkeit in festen Körpern und Gasen", Annalen der Physik **203**, 497–523 (1866).

[8]K. Bücks and H. Müller, "Über einige Beobachtungen an schwingenden Piezoquarzen und ihrem Schallfeld", Zeitschrift für Physik **84**, 75–86 (1933).

[9]T. G. Wang, "Acoustic levitation and manipulation for space application", The Journal of the Acoustical Society of America **60**, S21–S21 (1976).

[10]R. H. Morris, E. R. Dye, P. Docker, and M. I. Newton, "Beyond the Langevin horn: Transducer arrays for the acoustic levitation of liquid drops", Physics of Fluids **31**, 101301 (2019).

[11]M. A. B. Andrade, A. Marzo, and J. C. Adamowski, "Acoustic levitation in mid-air: Recent advances, challenges, and future perspectives", Applied Physics Letters **116**, 250501 (2020).

[12]A. Marzo, A. Barnes, and B. W. Drinkwater, "TinyLev: A multi-emitter single-axis acoustic levitator", Review of Scientific Instruments **88**, 10.1063/1.4989995 (2017).

[13]M. A. B. Andrade, N. Pérez, and J. C. Adamowski, "Review of Progress in Acoustic Levitation", Brazilian Journal of Physics **48**, 190–213 (2018).

[14]A. Marzo, S. A. Seah, B. W. Drinkwater, D. R. Sahoo, B. Long, and S. Subramanian, "Holographic acoustic elements for manipulation of levitated objects", Nature Communications **6**, 8661 (2015).

[15]V. Vandaele, P. Lambert, and A. Delchambre, "Non-contact handling in microassembly: Acoustical levitation", Precision Engineering **29**, 491–505 (2005).

[16]B. R. Wood, P. Heraud, S. Stojkovic, D. Morrison, J. Beardall, and D. McNaughton, "A portable Raman acoustic levitation spectroscopic system for the identification and environmental monitoring of algal cells", Analytical Chemistry **77**, 4955–4961 (2005).

[17]V. S. Jagadale, D. C. K. Rao, D. Deshmukh, D. Hanstorp, and Y. N. Mishra, "Modes of atomization in biofuel droplets induced by a focused laser pulse", Fuel **315**, 123190 (2022).

[18]A. Ashkin and J. M. Dziedzic, "Optical Levitation by Radiation Pressure", Applied Physics Letters **19**, 283–285 (1971).

[19]R. Loudon and C. Baxter, "Contributions of John Henry Poynting to the understanding of radiation pressure", Proceedings of the Royal Society A: Mathematical, Physical and Engineering Sciences **468**, 1825–1838 (2012).

[20]A. Ashkin, "History of optical trapping and manipulation of small-neutral particle, atoms, and molecules", IEEE Journal of Selected Topics in Quantum Electronics **6**, 841–856 (2000).

[21]A. Ashkin, "Acceleration and Trapping of Particles by Radiation Pressure", Physical Review Letters **24**, 10.1103/PhysRevLett.24.156 (1970).

[22]A. Ashkin, J. M. Dziedzic, J. E. Bjorkholm, and S. Chu, "Observation of a single-beam gradient force optical trap for dielectric particles", Optics Letters **11**, 288 (1986).

[23]J. Tello Marmolejo, B. Björnsson, R. Cabrera-Trujillo, O. Isaksson, and D. Hanstorp, "Visualization of spherical aberration using an optically levitated droplet as a light source", Optics express **28**, 30410–30422 (2020).

[24]S. Radhakrishnan, A. Alemán, P. Thazhath Bhaskaran, and D. Hanstorp, "Observation of FRET in collision of droplets", in Optical trapping and optical micromanipulation xvi, edited by K. Dholakia and G. C. Spalding (Sept. 2019), page 104.

[25]M. A. B. Andrade, N. Perez, F. Buiochi, and J. C. Adamowski, "Matrix method for acoustic levitation simulation", IEEE Transactions on Ultrasonics, Ferroelectrics and Frequency Control **58**, 1674–1683 (2011).

[26]T. Tuziuti, T. Kozuka, and H. Mitome, "Measurement of Distribution of Acoustic Radiation Force Perpendicular to Sound Beam Axis", Japanese Journal of Applied Physics **38**, 3297–3301 (1999).

[27]A. Crockett and W. Rueckner, "Visualizing sound waves with schlieren optics", American Journal of Physics **86**, 870–876 (2018).

[28]J. Jellstam, *Acoustic levitation as mobile visual representations*, MSc thesis (Gothenburg University, 2021).

[29]T. Kozuka, K. Yasui, T. Tuziuti, A. Towata, and Y. Iida, "Acoustic Standing-Wave Field for Manipulation in Air", Japanese Journal of Applied Physics **47**, 4336–4338 (2008).

[30]R. D. Muelas-Hurtado, J. L. Ealo, J. F. Pazos-Ospina, and K. Volke-Sepúlveda, "Acoustic analysis of a broadband spiral source for the simultaneous generation of multiple Bessel vortices in air", The Journal of the Acoustical Society of America **144**, 3252–3261 (2018).

[31]K. Hasegawa and K. Kono, "Oscillation characteristics of levitated sample in resonant acoustic field", AIP Advances **9**, 035313 (2019).

[32]R. D. Muelas-Hurtado, J. L. Ealo, and K. Volke-Sepúlveda, "Active-spiral Fresnel zone plate with tunable focal length for airborne generation of focused acoustic vortices", Applied Physics Letters **116**, 10.1063/1.5137766 (2020).

[33]S. Zehnter, M. A. Andrade, and C. Ament, "Acoustic levitation of a Mie sphere using a 2D transducer array", Journal of Applied Physics **129**, 134901 (2021).

[34]W. A. Oran, L. H. Berge, and H. W. Parker, "Parametric study of an acoustic levitation system", Review of Scientific Instruments **51**, 626–631 (1980).

[35]T. Kozuka, K. Yasui, T. Tuziuti, A. Towata, J. Lee, and Y. Iida, "Measurement and Numerical Calculation of Force on a Particle in a Strong Acoustic Field Required for Levitation", Japanese Journal of Applied Physics **48**, 07GM09 (2009).

[36]P. G. Bassindale, D. B. Phillips, A. C. Barnes, and B. W. Drinkwater, "Measurements of the force fields within an acoustic standing wave using holographic optical tweezers", Applied Physics Letters **104**, 163504 (2014).

[37]G. Thalhammer, R. Steiger, M. Meinschad, M. Hill, S. Bernet, and M. Ritsch-Marte, "Combined acoustic and optical trapping", Biomedical Optics Express **2**, 2859 (2011).

[38]G. Thalhammer, C. McDougall, M. P. MacDonald, and M. Ritsch-Marte, "Acoustic force mapping in a hybrid acoustic-optical micromanipulation device supporting high resolution optical imaging", Lab on a Chip **16**, 1523–1532 (2016).

[39]C. Fury, P. H. Jones, and G. Memoli, "Multiscale manipulation of microbubbles employing simultaneous optical and acoustical trapping", in Proc.spie, Vol. 9164, edited by K. Dholakia and G. C. Spalding (Sept. 2014), 91642Z.

[40]M. Kvåle Løvmo, B. Pressl, G. Thalhammer, and M. Ritsch-Marte, "Controlled orientation and sustained rotation of biological samples in a sono-optical microfluidic device", Lab on a Chip **21**, 1563–1578 (2021).

[41]J.-L. Thomas, R. Marchiano, and D. Baresch, "Acoustical and optical radiation pressure and the development of single beam acoustical tweezers", Journal of Quantitative Spectroscopy and Radiative Transfer **195**, 55–65 (2017).

[42]G. Gouesbet, "Generalized Lorenz–Mie theories and mechanical effects of laser light, on the occasion of Arthur Ashkin's receipt of the 2018 Nobel prize in physics for his pioneering work in optical levitation and manipulation: A review", Journal of Quantitative Spectroscopy and Radiative Transfer **225**, 258–277 (2019).

[43]D. Baresch, J.-L. Thomas, and R. Marchiano, "Three-dimensional acoustic radiation force on an arbitrarily located elastic sphere", The Journal of the Acoustical Society of America **133**, 25–36 (2013).

[44]M. Born and E. Wolf, *Principles of Optics*, 7th edition (Cambridge University Press, 2019).

[45]G. Pesce, P. H. Jones, O. M. Maragò, and G. Volpe, "Optical tweezers: theory and practice", European Physical Journal Plus **135**, 10.1140/EPJP/S13360-020-00843-5 (2020).

[46]P. H. Jones, O. M. Maragò, and G. Volpe, *Optical Tweezers* (Cambridge University Press, Dec. 2015).

[47]C. J. Price, T. D. Donnelly, and S. Giltrap, "An in-vacuo optical levitation trap for high- intensity laser interaction experiments with isolated microtargets", REVIEW OF SCIENTIFIC INSTRUMENTS, 10.1063/1.4908285 (2015).

[48]J. Marmolejo, A. Canales, D. Hanstorp, and R. Méndez-Fragoso, "Revealing Fano Combs in Directional Mie Scattering", preprint available, 10.21203/rs.3.rs-1100661/v1 (2021).

[49]A. Ashkin, "The pressure of laser light", Scientific American **226**, 62–71 (1972).

[50]D. T. Blackstock, *Fundamentals of physical acoustics* (John Wiley & Sons, 2000).

[51]H. Bruus, "Acoustofluidics 7: The acoustic radiation force on small particles", Lab on a Chip **12**, 1014 (2012).

[52]J. Lee and K. K. Shung, "Radiation forces exerted on arbitrarily located sphere by acoustic tweezer", The Journal of the Acoustical Society of America **120**, 1084–1094 (2006).

[53]L. P. Gor'kov, "On the forces acting on a small particle in an acoustical field in an ideal fluid", Soviet Physics Doklady **6**, 773–775 (1962).

[54]L. Lindahl, S. Furenäs, and T. Hainer, *Dynamics of Optically Levitated Micro-dumbbells*, technical report (Gothenburg University, 2021).

[55]Thorlabs, *PDP90A, 2D Lateral Effect Position Sensor, User Guide*, 2020.

[56]E.-L. Florin, A. Pralle, E. Stelzer, and J. Hörber, "Photonic force microscope calibration by thermal noise analysis", Applied Physics A: Materials Science & Processing **66**, S75–S78 (1998).

[57]*Personal communication with A. Johansson and R. Méndez-Fragoso about currently unpublished experimental and theoretical work on acoustic levitation*, 2022.

[58]M. A. B. Andrade, S. Polychronopoulos, G. Memoli, and A. Marzo, "Experimental investigation of the particle oscillation instability in a single-axis acoustic levitator", AIP Advances **9**, 035020 (2019).

[59]A. Lamprecht, S. Lakämper, T. Baasch, I. A. T. Schaap, and J. Dual, "Imaging the position-dependent 3D force on microbeads subjected to acoustic radiation forces and streaming", Lab on a Chip **16**, 2682–2693 (2016).